Final Report

U.S. Department of Energy Grant No. DE-FG02-95ER45540:

Stability of Bulk Metallic Glass Structure

Principal Investigators:

H. Jain and D.B. Williams
Department of Materials Science and Engineering
LEHIGH UNIVERSITY
Bethlehem, PA 18015

June 2003

The Structural Origins of the Stability of Pd-Ni-P Bulk Metallic Glasses

by

Faisal M. Alamgir

Presented to the Graduate and Research Committee
of Lehigh University
In Candidacy for the Degree of
Doctor of Philosophy

in

Materials Science and Engineering

Lehigh University

04-02-2002

Acknowledgements

I have many thanks for many people who have helped, encouraged, argued for, critiqued, my dissertation work to its completion. To preserve the sincerity of my words, I will make every attempt not to ramble.

I owe everything to my parents, for all their love and sacrifice for me. Tomader bhalobasha theke amar ei shikkhar jonmo; tomader doa'tie amar shikkha hobe poripurno.

Alena, my wife and closest friend, I thank for her unfettered belief in me. When my self-doubts would exceed all healthy limits, she carried me through with effortless grace. I am eternally indebted to her.

My advisors, Prof. Jain and Prof. Williams shepherded me through a rich graduate school experience. I am extremely grateful for their willingness to take risks with me when I had not yet proven myself. Through this liberal approach I was encouraged to visit ONERA, just outside of Paris, to perform experiments that pushed the boundaries of electron energy-loss spectroscopy (EELS). Later, when I felt it necessary to compare and complement my EELS studies with the more robust technique of X-ray absorption spectroscopy (XAS), they funded my work at the synchrotron source of the Brookhaven National Lab.

Outside of my advisors, I have had many informal mentors. Prof. Cargill had helped initiate me to working with synchrotron radiation. I thank him for this and for

the time he devoted to many discussions on the interpretations of XAS. Dr. Schwarz, I owe for bringing some order to my understanding of the disordered world of metallic glasses, and, indeed, for providing me with material samples. Dr. Gilles Hug of Onera saved me months of agony by helping me resolve the complexities of high quality EELS measurements of higher atomic number elements. I thank him for his hospitality during my stay in Paris.

I want to thank Prof. Klier for being an inspiration for me, both in the classroom and outside. He sets the standard for the scientist I want to become.

I want to thank all my friends from Lehigh for these and many inexpressible reasons: Pedja, for his loyal, quirky, warm friendship; Alex for her sincerity, and her selflessness; Eva, for all our conversations, laughs, and trips to the “Greasy Spoon”; Sumi, Gang, Anju, Keisha and Pradumnya, being much more than labmates (for example, by listening to me babble endlessly); I want to thank A.C. for introducing me to Prof. Klier’s classroom.

Maxine, Deanne, Arnita and Pat, have helped me work my confused self through the years. I am very grateful for all their help.

If you shut the door to all errors, truth will be shut out.

Rabindranath Thakur

TABLE OF CONTENTS

List of figures

Figure 6-1. The P and the Pd core-level spin-orbit split peaks, and only the $2p_{3/2}$ peak for Ni. Spectra were obtained for the alloys in Table 6-1, $Ni_{80}P_{20}$ glass and the Pd_3P crystal.

Figure 7-1: The Bernal holes showing the (i) tetrahedron, (ii) the octahedron, (iii) the trigonal prism, (iv) the tetragonal dodecahedron and (v) the Archmedian antiprism.

Figure 7-2: The trigonal prism is a naturally occurring structure in both Pd_3P and Ni_3P crystals. Here we see the Pd_3P structure where P sits in between two trigonal planes of Pd atoms and has three more Pd atoms laterally three half octahedral caps.

Figure 7-3: The valence band DOS of a) Ni, b)$Ni_{80}P_{20}$ glass, c) Pd, d) Pd_3P crystal, and e) $Pd_{40}N_{40}P_{20}$ glass. The spectra are scladed to match their maximum intensities.

Figure 7-4: The valence band for the $Pd_{40}Ni_{40}P_{20}$ glass calculated using the $Ni_{80}P_{20}$ starting structure in a locally self-consistent multiple scattering (LSMS) scheme[52]. The inset shows the Pd local DOS (LDOS) in this alloy . Clearly the result of alloying is a broadening of the d-band of Pd and that the state marked X originate from Pd.

Figure 7-5: A comparison of the valence band of $Pd_{40}Ni_{40}P_{20}$ and that of a simulated spectrum using a weighted average of $Pd_{60}Ni_{20}P_{20}$ and of $Pd_{30}Ni_{50}P_{20}$.

Figure 7-6: The P $2p_{3/2}$ core level positions of the glasses and crystals in the $Pd_xNi_{(80-x)}P_{20}$ glass.

Figure 7-7: Schematic showing the how creation of saddle points in the E-k dispersion can cause singularities in the DOS driving it away from the Fermi-Dirac ideal.

Figure 7-8: A schematic of the DOS of free electrons in a metal, and those in metallic glass and its corresponding crystal.

Figure 7-9: a) an example of the multiple fits carried out in order to avoid correlations, and b) the asymmetry parameter for the different alloy compositions.

Figure 7-10: V(r) for the molar volumes of $Pd_{60}Ni_{20}P_{20}$ and $Pd_{30}Ni_{50}P_{20}$ and $\bar{}$=1.8. The arrows mark the range of TM-P and TM-TM distances, Ni-P, Pd-P, Ni-Ni and Pd-Pd, respectively, for the Pd_3P and the Ni_3P alloys. The values are ~2.35 Å, 2.48 Å, 2.77 Å and 2.93 Å, respectively.

List of Tables

List of Abbreviations

BMG	bulk metallic glass
DOS	density of states
EELS	Electron energy-loss spectroscopy
EXAFS	extended X-ray absorption fine-structure
EXELFS	extended energy-loss fine-structure
|FT|	modulus of the Fourier transform
Im|FT|	imaginary part of the Fourier transform
PEELS	Parallel electron energy-loss spectroscopy
RDF	radial distribution function
TEM	transmission electron microscope
VEC	valence electron concentration
XPS	X-ray photoelectron spectroscopy

Abstract

The fundamental origins of the stability of the $(Pd\text{-}Ni)_{80}P_{20}$ bulk metallic glasses (BMGs), a prototype for a whole class of BMG formers, were explored. While much of the properties of their BMGs have been characterized, their glass-stability have not been explained in terms of the atomic and electronic structure. The local structure around all three constituent atoms was obtained, in a complementary way, using extended X-ray absorption fine structure (EXAFS), to probe the nearest neighbor environment of the metals, and extended energy loss fine structure (EXELFS), to investigate the environment around P. The occupied electronic structure was investigated using X-ray photoelectron spectroscopy (XPS). The $(Pd\text{-}Ni)_{80}P_{20}$ BMGs receive their stability from cumulative, and interrelated, effects of both atomic and electronic origin. The stability of the $(Pd\text{-}Ni)_{80}P_{20}$ BMGs can be explained in terms of the stability of $Pd_{60}Ni_{20}P_{20}$ and $Pd_{30}Ni_{50}P_{20}$, glasses at the end of BMG formation. The atomic structure in these alloys is very similar to those of the binary phosphide crystals near x=0 and x=80, which are trigonal prisms of Pd or Ni atoms surrounding P atoms. Such structures are known to exist in dense, randomly-packed systems. The structure of the best glass former in this series, $Pd_{40}Ni_{40}P_{20}$ is further described by a weighted average of those of $Pd_{30}Ni_{50}P_{20}$ and $Pd_{60}Ni_{20}P_{20}$. Bonding states present only in the ternary alloys were found and point to a further stabilization of the system through a negative heat of mixing between Pd and Ni atoms. The *Nagel and Tauc* criterion, correlating a decrease in the density of states at the Fermi level with an

increase in the glass stability, was consistent with greater stability of the $Pd_xNi_{(80-x)}P_{20}$ glasses with respect to the binary alloys of P. A valence electron concentration of 1.8 e/a, which ensures the superpositioning of the first peak in the structure factor with twice the Fermi momentum, was used to calculate the interatomic potential of these alloys. The importance of Pd to the stability of the alloys is evidenced by the fact that replacing Ni with Pd places the nearest neighbor distances at more attractive positions in this potential.

1 Introduction

1.1 Metallic Glasses

When we mention to almost anyone outside of the solid-state-science community that we study metallic glasses, we should do so with enough time in our hands. It may take some time to undo the experiential perceptions people have about "metals" and "glasses". Our experiences with metals are with wires and cables, load-bearing structures, tools, machinery, jewelry, etc. So, we think of a metal as being a good conductor of heat and electricity, hard and yet malleable and ductile, opaque, shiny and yet prone to tarnish over time. Similarly, from our experiences with glass as used in window panes, lenses, storage wares, insulation, cutting tools etc., we think of a glass as being transparent, poor conductor of heat, an electrical insulator, hard but brittle, ages well.

To the non-specialist, the properties of metals and glasses appear to be mutually exclusive! So, is a metallic glass a good conductor of electricity, or is it insulating? Can one see through a piece of metallic glass? How far can they be bent before they break? Metallic glasses behave very much like other metals in the sense that their electrical, magnetic and optical properties are very typical of metals, and yet, unlike traditional metals, which are crystalline, metallic glasses are amorphous. It is, then, the common perception of "glass" that needs to be challenged.

1.2 What is a Glass?

We all have a notion of what a glass is, but let us look at how it is defined by the Webster dictionary:

> *glass n. 1. Any of a large class of materials with highly variable mechanical and optical properties that solidify from the molten state without crystallization, that are typically based on silicon dioxide, boric oxide, aluminium oxide, or phosphorus pentoxide, that are generally transparent or translucent, and that are regarded physically as supercooled liquids rather than true solids.*

How can glass be "solidified" from the molten state but at the same time not be regarded as a solid but rather as a "supercooled liquid"? This dualism in the definition underscores some of the issues still being debated on the correct definition for glass. Some consider glass to be a liquid while others call it a solid, and some insist that glasses must be formed from the liquid phase in order to distinguish it from amorphous materials formed by vapor deposition or by sol-gel processing. It is perhaps best to define glass by its physical state rather than by its processing conditions or any composition-specific properties. A consensus can probably be drawn with the following two necessary qualities of a glass.

1. A glass is an amorphous material, meaning that, unlike a crystal, the atoms in glass are not arranged in a periodic lattice. The glass may have short-range ordering, that is, restricted to the first few nearest neighbor distances. An example of an exception to this general rule is the 6-membered boroxyl ring structure in glassy B_2O_3. Glass has a disordered atomic structure similar to

that of a liquid. A well-annealed glass with no residual stress is usually isotropic. The glass is a solid because its viscosity is on the order of 10^{15} Pa·s.

2. A glassy material is an amorphous solid that exhibits a glass transition. While all glasses are amorphous, all amorphous solids are not necessarily glassy. The glass transition is a second order phase transformation, which means that it is marked (as a function of temperature) by a discontinuity in derivative quantities (e.g., specific heat or thermal expansivity), that is, a change in slope of extensive thermodynamic quantities (e.g., volume or entropy).

As we see in Figure 1-1, the liquid can be cooled to either a crystal, or one of several metastable glassy states. The different solidification paths depend on the different cooling rates at used for the solidification process. If a glass is held at a temperature just below its glass transition temperature (T_g), it will eventually stabilize to the most stable of the possible glass structures. As we see in the figure however, depending upon the cooling rate, the T_g could be Tg1 or Tg3. Heating above T_g will drive the glass towards crystallization.

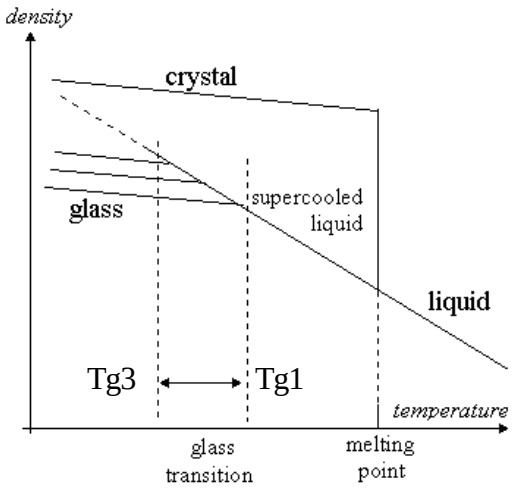

Figure 1-1: Density as a function of temperature showing the different states.

Although several glasses do exist in nature [1], naturally occurring metallic glasses have not been found yet. Metals, due to the relatively weaker chemical bonds between atoms, can easily seek out stable crystalline phases in short time scales. In fact, the discovery of metallic glass in the laboratory was serendipidous, at best [2].

1.3 Discovery of Metallic Glass

It was in the year 1959 that Pol Duwez found a non-equilibrium crystalline phase in the Ag-Ge system as it was cooled very rapidly from the liquid state. Sensing that he was onto something that transcended the particulars of the Ag-Ge system, he chose to explore the chemically similar Au-Si system. The X-ray diffraction pattern for the rapidly solidified $Au_{80}Si_{20}$ alloy, however, showed no evidence of any crystallinity at all. Duwez had accidentally discovered the first

amorphous metal quenched from the liquid state [2]. Soon afterwards, Cohen and Turnbull pointed out that this amorphous alloy composition was near that of a very low melting eutectic point in the equilibrium phase diagram [3], a favorable condition for glass formation in ionic glasses. This simple criterion led to the discovery of another amorphous metal system, the $Pd_{80}Si_{20}$ alloy. The question as to whether these were amorphous metals or metallic glasses was answered when these alloys were shown to exhibit a glass transition.

Next, attention was paid to bulk amorphous alloys with low critical cooling rates for glass formation. It was found that the $Pd_{40}Ni_{40}P_{20}$ and $Pd_{76}Cu_6Si_{18}$ glasses could be produced by water quenching to diameters up to 3 mm and 0.3 mm, respectively [4,5]. Subsequently, a flux treatment using a B_2O_3 medium was effective in increasing the maximum sample thickness for the Pd-Ni-P alloy during glass formation to about 10 mm [6, 7]. Until the 1990s, there was a long period in which no bulk glassy alloys except for the Pd-Ni-P and Pt-Ni-P systems were known. All of the other metallic glasses known at the time required high cooling rates - on the order of 10^6 K/s.

Over the last decade, various alloy systems have been found which can lead to bulk glass formation. To name a few representative systems we will categorize the glasses into two families, those glasses which contain only metals versus those which contain metals and metalloids. Examples of glasses containing only metals are the Mg-Ln-TM (Ln=Lanthanum, TM=Transition Metal) [8], Nb-Fe-Al [9] and Zr-Al-TM [10] systems. Those which contain both metals and metalloids are, for example, the

Zr-Ti-TM-Be [11], the Pd-Cu-Ni-P [12], and the Pd-Ni-Fe-P [13] systems. Of these glasses, the $Pd_{40}Ni_{10}Cu_{30}P_{20}$ is the current record-holder for being the bulkiest. It has a minimum dimension of 72 mm at room temperature.

What are the properties of interest in metallic glasses, and why is there so much interest in preparing them in the bulk form?

1.4 Properties of Metallic Glasses

Because metallic glasses lack crystalline structure, they also lack crystalline defects, such as grain boundaries and dislocations. Without these defects, metallic glasses can have extraordinary mechanical properties such as high strength, high corrosion resistance and soft magnetic properties.

The corrosion resistance can be understood from the fact that there are no crystalline grains present in the glass, and therefore no weak grain boundaries for chemical attack. One may say that there are grain boundaries present but that they are at a nanometer scale since there may be well defined (crystal-like) local atomic structure. The counter-argument for this is that these (pseudo) grain boundaries provide a more circuitous path for corrosion in comparison to polycrystalline materials. More rigorously, the ("grain boundary" surface area)/(grain volume) is much larger for the metallic glass than its polycrystalline counterpart, so that less volume of material is removed per grain boundary area during chemical attack. This idea has already been commercialized. For example by Karta Technologies, Inc.

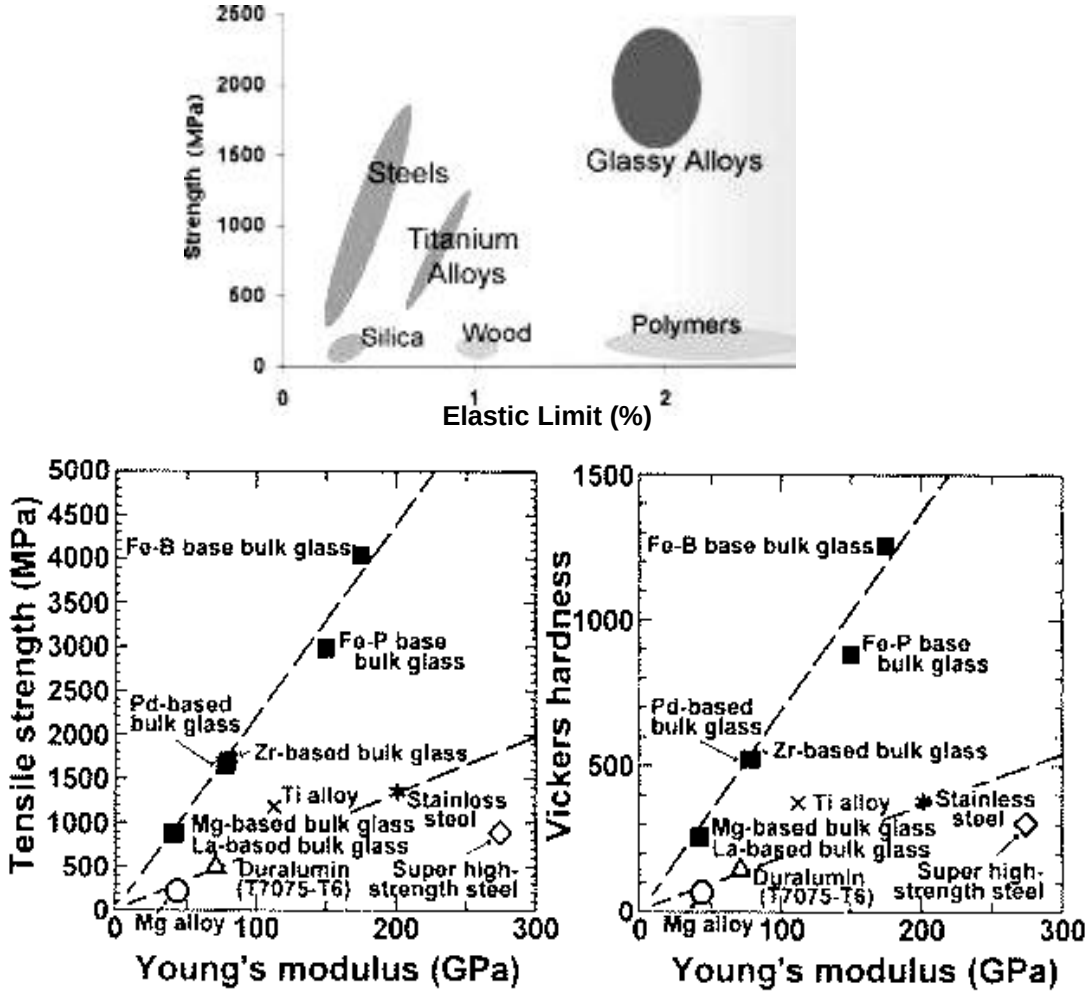

Figure 1-2: The unique blend of high strength and high elastic limits in metallic glasses [ref: http://www.er.doe.gov/feature_articles_2001/June/Decades/26.html] in comparison to various other materials. The tensile fracture strength and the Vickers hardness for typical bulk metallic glass are also shown in comparison with those of typical crystalline alloys[14] .

has used rapidly solidified metallic glass structures in surface layers of steel superheater tubing coal-fired power plants. Coal ash corrosion is a leading cause of failure in tubes made of austenitic steels. The development of these corrosion-resistant glass coatings can have a significant impact on the electrical utility industry

by saving the materials costs involved in replacing superheater tubes, reducing downtime, and reducing the probability of a catastrophic failure.

The mechanical properties of metallic glasses combine the high strength of steels with the high elastic limit of polymers (Figure 1-2) [14]. This means that large amounts of elastic energy can be stored in metallic glasses, which is released with complete recovery of the original material. This, combined with the high fracture tensile strength makes metallic glass an excellent candidate for tools for cutting or writing, springs, sporting goods, etc. Indeed, the first commercialization of bulk metallic glasses has been of golf clubs!

1.5 Bulk Metallic Glass

Over the last decade there has been a rapid expansion in the field of metallic glasses with the discovery of processing techniques and alloy compositions that allow bulk glass formation [15, 16]. A distinction should be drawn now between a metallic glass in general, and a bulk metallic glass (BMG).

There is really no agreed standard for what minimum dimension graduates a metallic glass to a BMG. Yet, it is tacitly accepted that a BMG should have a minimum dimension > 1mm. There is no real logic for making this delineation, except for the fact that it cleanly separates the regime of binary metallic glasses from those (in the right composition) containing more constituent elements. For example, an alloy of Pd, Ni, Cu or binary alloys of transition metals (Pd, Ni, Cu, etc.) and

metalloids (P, Si, etc.) do not form BMGs, their minimum dimension remaining < 1mm, or conversely, requiring critical cooling rate > 10^3 K/s. The Pd-Ni-P system on the other hand has a critical cooling rate lower than 1 K/s and, as mentioned above, can have a minimum dimension of a centimeter. Experience has shown that at least 3 elements are needed to produce glasses of minimum dimensions > 1mm.

At the minimum thickness of BMG, the high strength and high elastic limits of metallic glass can be taken advantage of over larger dimension of devices. As mentioned before, the first commercialization of a BMG was in the manufacture of golf clubs, taking advantage of a highly elastic club/ball collision and therefore a very efficient transfer of the energy that is stored on a swing.

Hand in hand with a large minimum dimension is of course a low critical cooling rate for glass-formation. A low critical cooling rate, furthermore, implies that the glass forming system has a wide temperature range where it is below the melting temperature, but still remains a liquid. Conversely, as the glass is heated to above T_g, the temperature range over which the glass will remain a supercooled liquid before it crystallizes at T_x, will be correlated to the minimum dimension of the glass. This is what we can say intuitively, and, in fact, that is borne out empirically [17] . It is found that linearly correlated with increasing temperature range of the supercooled region (T_x-T_m) is the minimum dimension of the solid glass [Figure 1-3].

With this large supercooled region, which was not available in for the binary metallic glasses, it has become feasible to implement net-shape forming technology of

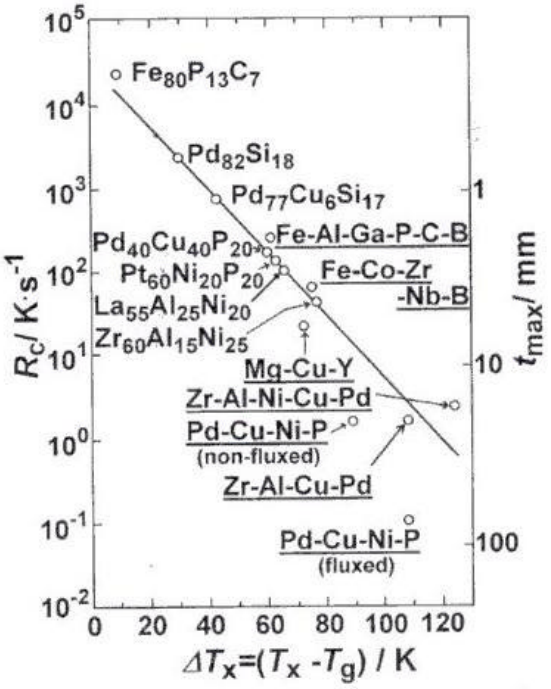

Figure 1-3: The relationship between the maximum thickness (t_{max}), the critical cooling rate (R_c) and the width of the supercooled region ΔT_x. Data compiled by Inoue [17]

glass manufacture to the manufacture of metals. Glasses can now be heated to a point above T_g but below T_x, the supercooled liquid be allowed to flow and then cooled back to a glass, thus allowing the casting to take place at a temperature much lower than the melting temperature. This has significant cost-saving implications, for example in the production of complex shapes by direct casting, without the need for expensive machining.

2 Objective: A Study of the Stability of Bulk Metallic Glasses

The promise of a host of new combination of properties in a bulk glassy alloy has motivated extensive work over the past decade towards the discovery of new BMG systems. Much of the attention in research has been given to increasing the minimum dimensions in these glasses while keeping the materials cost down, and in tailoring their properties by the addition of new constituent elements. The result has been that BMG systems have become increasingly complex, with 5 or 6 constituent elements not uncommon.

However, very little attention has been given to developing fundamental understanding of how the atomic and electronic structure drive the stability of the glass. Some empirical rules have been developed over the years. Glass stability has been explained to some extent by different criteria that are based on the suppression of the nucleation of crystals [18], the suppression of the kinetics via the "confusion principle" [16], and atomic size effects of the constituent elements [19]. Yet, the same question has not been adequately addressed from the viewpoint that the stability of the glassy phase originates from a combined contribution of the atomic and electronic structure of the system. Since the "bulk" nature of new glassy alloys is central to the rejuvenated scientific interest in them, a basic question needs to be answered: what determines their easy glass forming ability or the stability of the glassy phase in general? What are the origins of these empirical rules for bulk glass formation from the point of view of atomic and electronic structure? We propose to answer these

questions. To achieve this, we selected a model BMG system and investigated its atomic and electronic structure.

2.1 The Pd-Ni-P BMG System

The Pd-Ni-P alloy system is the simplest prototype of a BMG [20]. With three constituent elements a study of the structure of these glasses remains tractable in comparison to other BMGs that often contain five or more elements. This system offers a wide range of bulk glass formability, with $Pd_{40}Ni_{40}P_{20}$, as the most stable glass composition in the Pd-Ni-P series [21]. It is being used as a starting structure for bulk glasses in which the properties can be tailored by the substitution of Pd and Ni by other transition metals. For example, Shen et al. [22] have found that by substituting the Ni with Fe, the paramagnetic $Pd_{40}Ni_{40}P_{20}$ glass can be transformed to exhibit superparamagnetic, ferromagnetic and spin-glass behavior depending on the temperature and the applied magnetic field.

Bulk glass formability of Pd-Ni-P centers around a narrow range of P concentration of about 20% [23]. Attempts to construct the structure of Pd-Ni-P glasses have, therefore, concentrated on the binary crystalline phases closest to $Pd_{80}P_{20}$ and $Ni_{80}P_{20}$, viz. the low symmetry Pd_3P and Ni_3P crystals. It is known that the crystalline Ni_3P and the Pd_3P phases contain tetradecahedral structural motifs [24, 25 respectively], which can best be described as trigonal prisms in which the three square faces are capped by half octahedra, with P sitting in the center of the prism. This

structure was found by Bernal [26] from the analysis of his model of dense random packing of hard spheres (DRP). Cargill [27] found the structure of *glassy* $Ni_{76}P_{24}$ to be very close to that of DRP indicating a close structural link between the crystal and the glassy structure of Ni_3P. Maitrepierre [28] studied thin foils of $Pd_xNi_{(80-x)}P_{20}$ glasses, with x=32-73, and found that their structure compares well with that of a model structure of a Pd rich Pd_3P. More recently, Otomo *et. al*. [29] found by neutron inelastic scattering that the vibrational modes of the $Pd_{40}Ni_{40}P_{20}$ glass are best modeled by fundamental units of the trigonal prism symmetry (D_{3h}), once again pointing to Ni_3P and Pd_3P- like local environment in the BMG.

We shall investigate the applicability of Pd_3P and Ni_3P motif in describing the structure of $Pd_xNi_{(80-x)}P_{20}$ glass. This will be done by examining both the atomic and electronic structure, and their inter-relationship. Further, we shall attempt to study the glass stability in this prototypical system by observing at the changes in the structural features upon crystallization. Some general criteria for glass stability will be developed on the basis of our findings.

2.2 Structural Probes

We have chosen three techniques to examine the electronic structure and the atomic structure of the $Pd_xNi_{(80-x)}P_{20}$ glass. The occupied electronic structure was examined by X-ray Photoelectron Spectroscopy (XPS). The atomic structure was examined by extended X-ray absorption fine structure (EXAFS) and, its electron

analog, the extended energy loss fine structure (EXELFS), in order to reveal the partial radial distribution function (PRDF) of atomic neighbors around a central atom. The word "partial" here indicates that the results are specific to the element involved in the ionization process.

2.2.1 EXAFS and EXELFS

The fact that EXELFS and EXAFS provide element-specific PRDFs gives them an advantage over X-ray diffraction, which yields only an averaged total RDF. This feature allows even complex multi-component structures to be determined, if the information around all the elements is accessible. With chemical and isotopic substitution, partial structure factors can be obtained also from X-ray and neutron diffraction, respectively. However, since no such substitution in the system is required in order to get partial structural information, the combination of EXAFS and EXELFS, remains a powerful set of experimental probes into the atomic structure.

EXAFS has been studied extensively in the past [30, 31, 32]. EXELFS, on the other hand, has received very limited attention because poor counting statistics and the possibility of beam-damage from prolonged irradiation have discouraged the development of this technique to its full potential. This is unfortunate, since, in fact, EXELFS carries a niche in that it is particularly suitable for the study of low atomic number elements, where EXAFS has difficulties.

As the synchrotron X-rays do in EXAFS, in EXELFS the incident electron beam in a transmission electron microscope (TEM) ionizes an atom and the resulting

ejected electrons occupy energy levels in the conduction band of the sample. However, accessing the K-edges below 3 keV becomes problematic in EXAFS since absorption at these energies requires sub-micron sample thickness for transmission. Fluorescence EXAFS is possible for low atomic number elements, but that requires placing the sample chamber in vacuum, something most EXAFS end-stations are not set up for. Since the incident electrons in a TEM can be focused with magnetic lenses, EXELFS offers the unique ability to obtain atomic and electronic structure on a nanometer-scale spatial resolution. Further, since TEMs operate in high vacuum and use thin specimens, EXELFS is especially suited to K-edge analysis of low atomic number elements.

EXELFS is obtained from an electron energy-loss spectroscopy (EELS) spectrum. Downstream from the sample in a TEM, the Parallel Electron Energy-Loss Spectrometer (PEELS) provides a unique capability of acquiring information on the atomic structure. EELS provides a unique capability of acquiring information on the atomic and electronic structures on a nanometer-scale, manifested as fine structures appearing on ionization edges of the element of interest. When the incident electron beam ionizes an atom in a sample, the resulting ejected electrons occupy energy levels in the conduction band of the sample and thereby modulate the energy loss characteristics of the incident electrons. In electron energy-loss spectroscopy these modulations appear as oscillations beyond the ionization edge. In the first 50 eV beyond the edge, the ejected electrons probe the chemical bonding states that appear as the energy-loss near-edge structure (ELNES). The modulations at higher energies,

the extended energy loss fine structure (EXELFS), reflect the interactions between the ionised electron and the potentials of surrounding atomic neighbours. The X-ray absorption analogy is, of course, XANES and EXAFS.

The EXELFS and EXAFS oscillations can be expressed as a function of k, the momentum transferred to the ionised electrons. This function, $\chi(k)$, has the following form for a Gaussian pair distribution function [33, 41]:

$$\chi(k) = \sum_j \frac{N_j}{r_j^2} S_0^2 * \frac{F_j}{k} \exp(-2r_j/\lambda) \exp(-2\sigma_j^2 k^2) \sin[2k * r_j + \phi(k)] \qquad [2.1]$$

where F_j is the backscattering amplitude, S_0 is the many-electron overlap factor (also known as the amplitude reduction factor) from shake-up or shake-off effects of bound electrons, λ is the mean-free-path of the photoelectron through the medium, $2\sigma_j^2$ is the Debye-Waller factor, and $\phi(k)$ is the phase shift between the outgoing and backscattered photoelectrons. N_j is the number of neighbors in a shell of atoms at a distance r_j, and N_j/r_j is the Gaussian approximation of the partial radial distribution function (PRDF).

The useful momentum range that is accessible using EXAFS and EXELFS is less than that of X-ray or neutron scattering. This is because in diffraction the information begins from zero momentum transfer, q=0, whereas in EXAFS and EXELFS the information at low mementum transfer, $k \leq 2.5$ Å^{-1} is not used because in this range it is susceptible to multiple scattering effects. We have used both q and k to

refer to momentum transfer. They are, of course, related, and the different symbols stem from the different conventions adopted by the diffraction and the EXAFS communities. In the case of the latter, the scattering path of the radiation is a round trip. We see this in the Fourier component of $\chi(k)$, which is (2k*r), whereas in diffraction experiments it is (q*r). The range of 2k in EXAFS experiments is less than twice that of q in diffraction experiments; $2.5 \leq 2k \leq 30$ $Å^{-1}$ whereas $0 \leq q \leq 15$ $Å^{-1}$ [34]. This, therefore, renders the (k*r) factor to be slightly less than (q*r) and so the amount of information obtained from EXAFS is less than from diffraction.

This shorter momentum range limits the resolution of the distribution function in real space. This can be a costly problem, especially in the determination of the structure of a system that is inherently disordered. For the most part, though, one has to be satisfied with a semi-quantitative or even a qualitative description of the structure. This can be done by the direct interpretation of the real-space or momentum-space distribution functions as long as one takes into account the contributions from the changes in phase shifts and scattering amplitudes. In order to get more quantitative information, one can perform a least-squares fit of the experimentally derived distribution function with that which is calculated for a model system. This scheme is wrought with complications for systems with low symmetry, such as the Pd_3P crystal. In a later chapter we shall make a case study of quantitative EXAFS of the Pd_3P crystal, and attempt to modify the model to the Pd-Ni-P glass system.

2.2.2 XPS

XPS was born out of two Nobel Prize winning bodies of work. The first is the photoelectric effect, for which Albert Einstein received the Nobel prize in 1921. The second is for the work by Kai Siegbahn and his research group who developed the technique in the mid 1960s. Siegbahn was awarded the Nobel Prize for Physics in 1981 for his work on XPS.

The process of photoionization can be considered in the following way:

$$X + h\nu \rightarrow X^{+} + e^{-}$$

Conservation of energy then requires that :

$$E(X) + h\nu = E(X^{+}) + E(e^{-})$$

The final-state energy of the photoelectron at the vacuum level, $E(e^{-})$, is the "kinetic energy" measured by the detector, which, of course, has the work function, w, of the detector added to it. So, the kinetic energy measured by the detector, is given by $K = E(e^{-}) + w$ and so:

$$K = h\nu + w - [\, E(X^{+}) - E(X)]$$

The final term in brackets, representing the difference in energy between the ionized and neutral atoms, is generally called the binding energy (B) and so:

$$B = h\nu + w - K$$

For XPS, hν is usually 1486.6eV (Al Ká) or 1253.6eV (Mg Ká). The XPS technique is highly surface specific due to the short range of the photoelectrons that are excited from the solid, and w does not need to be explicitly known, since it only provides a constant shift to the scale. One might ask about the work function of the sample itself. Since work function is dependant on the composition of the sample, how can compositionally different samples be compared on the same scale without explicit knowledge of the samples? The answer is simple. The amount of kinetic energy lost due to the work function of the sample as the electron is leaving is regained when the electron is entering the detector. Since the detector work function is a constant, the binding energy comparisons of compositionally different samples remains valid.

The value of B is unique for most transitions of elements in their elemental state, and so deviations of the value of B (observed as the maximum in a peak-shape) from these standard values indicate deviations in chemical environment. The shape of the peaks can also change with subtle changes in chemical environment.

The value of K=0 is usually chosen by the Fermi level of a metal standard used and the experiment is conducted with the Fermi level of the sample in equilibrium

with that of this standard. The inflection point on the top of the valence band of this standard metal is typically chosen as the Fermi level.

3 Experiments

Three different structural probes were used to examine the electronic and the atomic structure of Pd-Ni-P alloys. Extended X-ray absorption fine structure (EXAFS) and its electron counterpart, extended energy-loss fine structure (EXELFS) were used to study the atomic structure while the valence and core-level electronic structure was probed using X-ray photoelectron spectroscopy (XPS). Bulk samples of glassy $Pd_{30}Ni_{50}P_{20,}$ $Pd_{40}Ni_{40}P_{20}$, $Pd_{60}Ni_{20}P_{20}$ and Pd_3P alloys were prepared by water quenching the melt. The details of the processing of the alloys can be found elsewhere[35]. Thin foils of glassy $Ni_{80}P_{20}$ were prepared by an autocatalytic reaction between $NiSO_4.2H_2O$ and $Na_2H_2PO_2$ [36].

3.1 EXAFS

3.1.1 Sample Thickness

In the transmission EXAFS experiment, the flux of X-rays incident on the sample is monitored by the current in an ionization chamber (I_0) (see Figure 3.1), and the flux of x-rays transmitted through the sample is measured by a second ionization chamber current (I_t). If the sample is of uniform thickness x, the x-ray absorption coefficient $\mu(E)$ of the sample is given by $I = I_0 \exp(-\mu x)$, or $\mu x = \ln(I_0/I_t)$. Downstream from chamber measuring I_t the beam can transmit through a reference

and then enter a third ionization chamber (measuring I_r). This is useful to have for energy calibrations. The μ(E) of the reference is calculated in the same way as for the sample, with the I_t and I_r replacing I_0 and I_t in the equation above.

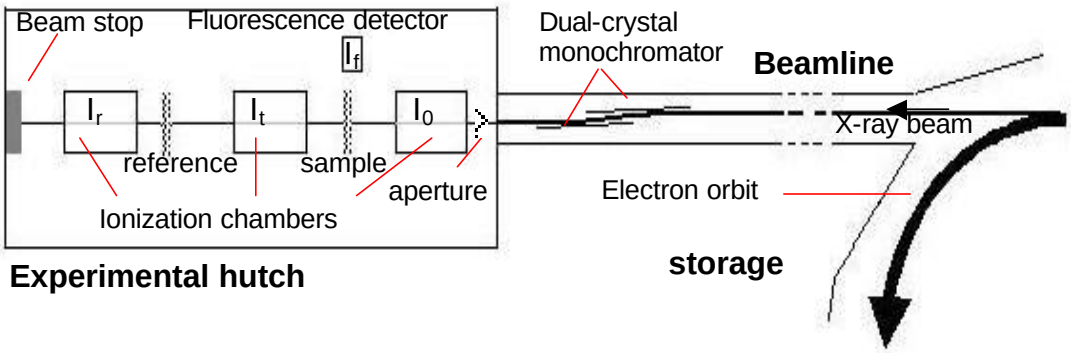

Figure 3-1: A schematic showing the experimental setup at a synchrotron beamline.

The absorption coefficient, μ(E), is related to the cross-section σ (cm^2/g) and the density ρ (g/cm^3) by $\mu = \sigma\rho \approx \sigma_i\rho_i = \rho \Sigma_i (m_i/M) \sigma_i$. The factor m_i/M is the weight fraction of the element i in the sample. The sample thickness required can therefore be calculated as:

$$x = \ln (I_0/I_t)/ \{\rho \Sigma_i (m_i/M) \sigma_i\}$$

to satisfy that the value of $\ln (I_0/I_t)$ be close to 1 which allows a significant change in absorption across the edge (edge step) but also enough transmission of X-rays through the sample for that change to be observed. The calculated thickness for the Pd and Ni K-edge energies for each sample are given below in Table 3.1:

Table 3-1: The thickness in cm of the samples in cms

	Pd edge	Ni edge
Pd_3P	0.01166	
$Pd_{60}Ni_{20}P_{20}$	0.01012	0.00053
$Pd_{40}Ni_{40}P_{20}$	0.00879	0.00047
$Pd_{30}Ni_{50}P_{20}$	0.00815	0.00044
$Ni_{80}P_{20}$		0.00036

3.1.2 Sample Preparation

Bulk samples were thinned down to the appropriate thicknesses for transmission experiments, by grinding and polishing. The Dimpler (described below), an instrument that is very useful for automated thinning of a selected region down to the order of tens of microns, came in very useful for creating areas of different thickness within one freestanding sample. This allowed for EXAFS experiments to be conducted at different K-edge energies on the same sample while maintaining the appropriate thickness for those energies (Figure 3-2).

As we can see from Table 3.1 the ideal thickness for the Pd edge for all the

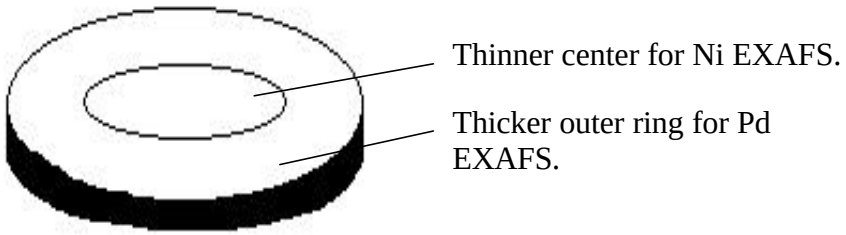

Figure Figure 3-2: A schematic of a bulk sample for transmission EXAFS experiments with regions of differing thickness.

samples is about 20 times that for the Ni edge. Lacking the precision in polishing controls beyond ~ 2 ìm when using the Dimpler, and ~ 5 ìm when using hand polishing, the Pd edge parts of the samples were thinned to about 90 ìm, while the Ni parts were thinned to approximately 5 ìm.

For fluorescence detection, the samples were not thinned since it is a surface technique. In this case, care was taken to ensure that the bulk samples were polished with a fine abrasive (1 μm diamond paste) for , and that the powdered samples were of fine particle size (400 mesh) .

Glass samples were crystallized ex-situ in a quartz tube under N_2 atmosphere. The samples were heated up to the crystallization temperature (T_x), held at T_x for an hour, and then cooled back down to room temperature before they were removed from the N_2 atmosphere.

3.1.3 Data Collection

K-edge EXAFS of $Pd_{30}Ni_{50}P_{20,}$ $Pd_{40}Ni_{40}P_{20}$, $Pd_{60}Ni_{20}P_{20}$, Pd_3P and $Ni_{80}P_{20}$ were measured in transmission at the X23A2, X15B and the X18B beamlines of the National Synchrotron Light Source at Brookhaven National Laboratory. The beamlines were equipped with Si (311), Si (111), and Si (111) mochromator crystals, respectively. Data were processed using the WinXAS 97 software [39]. The process consisted of a background subtraction, conversion of data from energy space to k space, isolation of the oscillation, and weighting by k^n to correct for the decaying of the amplitude. Further, the function $\chi(k)k^n$ was multiplied by a square-Gaussian

envelope function, to eliminate artifacts of the subsequent Fourier transformation, FT[$k^n * \chi(k)$]). FT[$k^n * \chi(k)$]) is proportional to the partial radial distribution function, or the statistical distribution of atomic neighbors, around the central atom being probed.

3.2 EXELFS

3.2.1 Sample Preparation

For EXELFS, the transmission electron microscope samples of the alloys $Pd_{30}Ni_{50}P_{20,}$ $Pd_{40}Ni_{40}P_{20}$, and $Pd_{60}Ni_{20}P_{20}$ were prepared in the following way:

1. First, cross-sectional discs (~ 1 cm diameter) were cut from the sample rods to thickness below 0.3 mm using a Struers Acutom 50. The discs were then tripod polished with 3 μm diamond paste down to the range of 50-100 μm sample thickness.
2. Smaller discs of 3mm diameter (the standard size for samples in TEMs) were punched from the samples and were then thinned to ~ 10 μm using a VCR Group Inc. D500i Dimpler.
3. The samples were then thinned down to electron transparency using a GATAN 691 Precision Ion Polishing System. A low accelerating voltage of 3-4 keV and a shallow incident angle were used for the beam of Ar ions. A thickness of $0.2*\lambda_i$ was obtained, where λ_i is the inelastic mean free path (~ 50 nm), under a 350 kV beam.

3.2.2 Data Collection

A JEOL 4000 FX microscope was used for acquiring P K-edge electron energy-loss (EEL) spectra with a parallel EEL spectrometer (Gatan 666 PEELS) at ~100 K sample temperature and using a 350 keV source. EELS was carried out indiffraction mode, meaning that a diffraction pattern was at the plane of the objective aperture. In this mode, the collection angle, β, which is the angle over which the scattered beams are collected by the PEELS spectrometer (Figure 3-3), is controlled by the size of the entrance aperture to the spectrometer, and the camera length, L, which is the distance between the specimen and the viewing screen in a microscope. In order for β to be large enough to capture all those electrons which suffered up to a specific energy loss, an appropriate range of values for L can be calculated using the relation:

$$\beta = (2E/\gamma m_0 \nu^2)^{1/2} \approx d/L$$

where d is the aperture size, γ is the relativistic factor and ν is the velocity of the high voltage electrons, and E is the energy-loss of interest. For energy losses in the range of the P-K-edge, a relatively low camera length (< 800 mm) had to be used while using the largest entrance aperture (5 mm).

3.2.3 Data Extraction

Dark counts were subtracted from the raw spectra. Channel-to-channel gain variations were removed by dividing the spectrum with the difference function

between the pre-edge background and a power-law fit of this background.

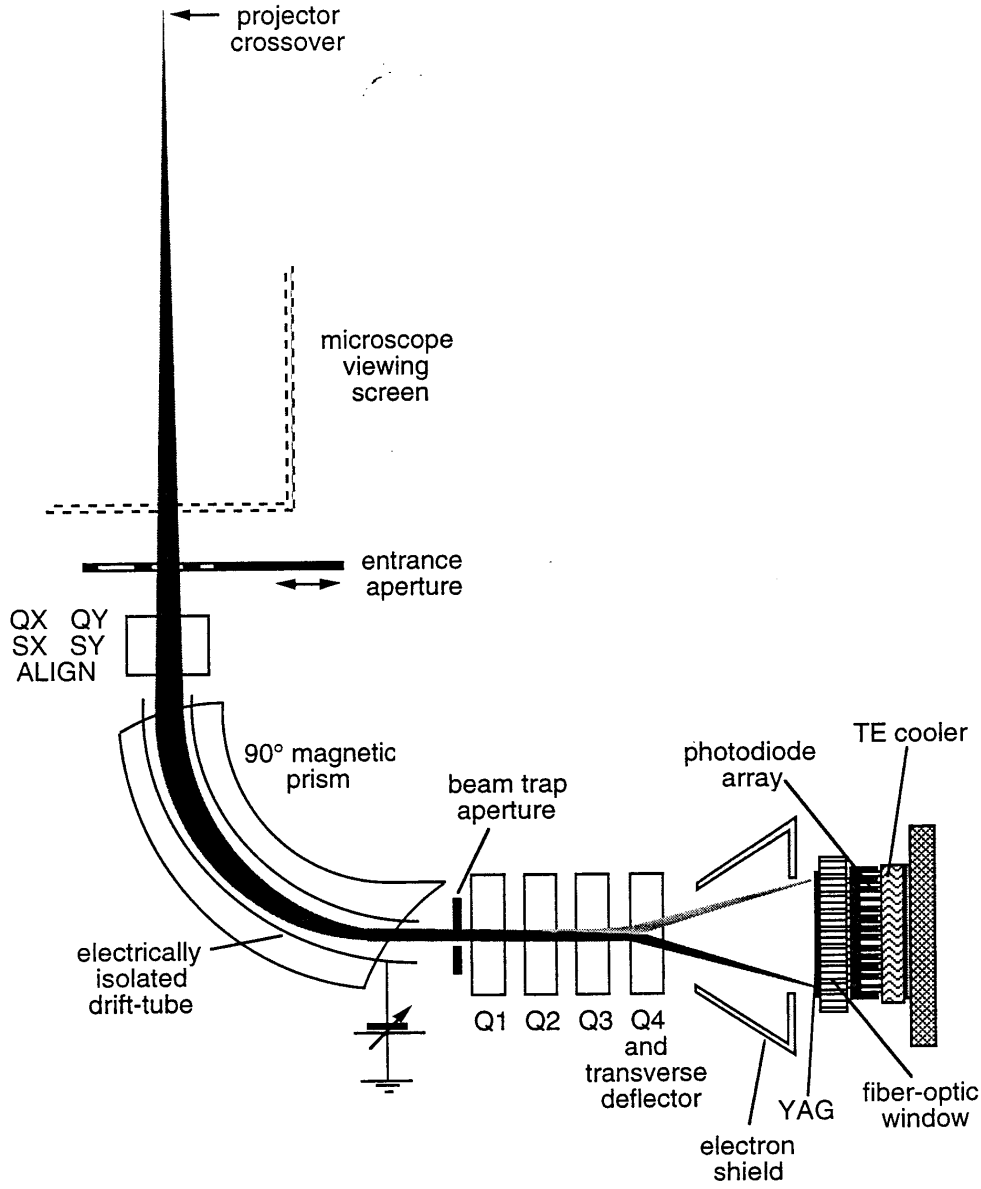

Figure 3-3: A schematic of the PEELS system, showing the path of the inelastically scattered electrons from the microscope to the detector

Contribution of plural scattering (defined as the case when greater than 1 but less than twenty 20 scattering events occur by the incident beam) [37] was removed by applying

the Fourier-ratio deconvolution (Egerton, 1996). The remaining data processing is common to both EXELFS and EXAFS.

3.3 XPS

Core-level and valence-band XPS spectra were obtained for all the samples with a Scienta ESCA-300 spectrometer using Al Kα (1486.7 eV) x-rays, with a rotating aluminum anode and a high-resolution hemispherical electrostatic analyzer. The surface of each specimen was mechanically cleaned in high vacuum (10^{-7} Pa) with a diamond tool before recording a spectrum. The Fermi energy of Ag was used as zero on the binding energy scale, and the Fermi levels of the samples were in equilibrium with that of Ag through proper electrical contact.

The spectra were acquired and analyzed using the WinESCA software. Whenever the background was isolated from any peak, a Shirley [38] background was chosen and fitted over a suitable energy range encompassing the peaks.

4 EX(AFS/ELFS) Data Reduction and Its Effects

EXAFS and EXELFS data were processed using the WinXAS 97 software [39]. The process consisted of a background subtraction, conversion of data from energy space to k space, isolation of the oscillation, weighting of the function $\chi(k)$, and the subsequent Fourier transformation to real space. FT[$k^n * \chi(k)$]) is proportional to the partial radial distribution function, or the statistical distribution of atomic neighbors, around the central atom being probed.

4.1 Data Reduction

WinXAS 2.1 package was used for data processing. The program performs the following steps:

1. A pre-edge and a post-edge background subtraction using a 1st order polynomial for the pre-edge and a low order polynomial for the post-edge (1st or 2nd order).
2. Conversion from energy space to k-space. The magnitude k of the wavevector of the ejected electron is given by:

$$k = 2p / l \cong \left[2m_0 E_{kin}\right]^{1/2} / \hbar = 5.123\left(E - E_0\right)^{1/2}$$

where E_{kin} is the kinetic energy of the ejected inner-shell electron and E_0 the energy corresponding to $E_{kin} = 0$. Here, the inflection point of an edge was taken as E_0.

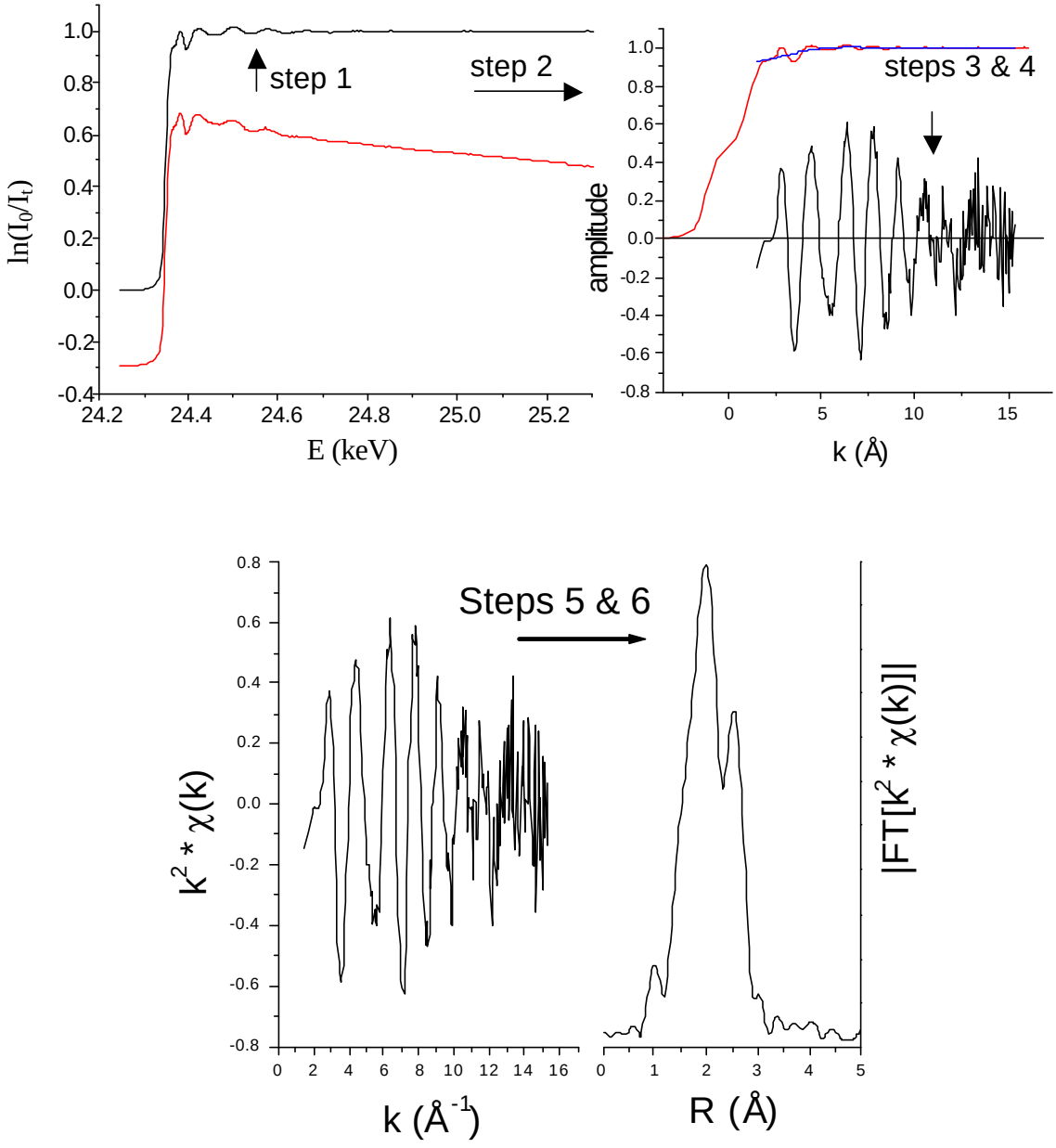

Figure 4-1: A flow-chart showing the first six steps of data treatment of EXELFS and EXAFS spectra.

3. Isolation of oscillatory component of EX(AF/ELF)S (χ(k)function) by using a cubic spline function, which is a cubic function with nodes, where the number of nodes can be chosen. The k-range of the data is divided into several regions, and separate cubic polynomials are fit to the data over each region. The cubics are constrained so the values, and the first and second derivatives match at the nodes.

4. Correction for k-dependent decaying of the amplitude of backscattering by weighting χ(k) with k^n.
5. Damping both ends of k-range of interest χ(k) by multiplying an appropriate background function. A square Gaussian function was used to achieve this.
6. Fourier transform of χ(k) to real space FT[k^n * χ(k)]).
7. Correction for phase shifts. If the phase shift function $f(k)$ can be approximated as a linear function of k, $f(k) = f_0 + kf_1$, the *r*-value corresponding to each Fourier transform, FT, peak increases by $|f_1|$. Tentative phase-shift correction can be applied qualitatively by using the above equation and assuming the phase shift is linear in k-space. This does not need to be done if only experimental spectra are compared and it is believed that the backscattering phase does not change much upon composition change.

8. Finally, the FT[k^n * χ(k)] is fitted with that of a model system using an ab initio code.

4.2 The Effects of Each Data Reduction Step

We shall now examine in more detail the effects of the various parameters on the data reduction scheme. Please refer to D.E. Sayers and B.A. Bunker [40] for further reading on this topic.

4.2.1 Normalization

In EXAFS experiments, the exact concentration of the absorbing atom is often not known and also a variety of materials such as the detector windows, and the sample matrix itself add unknown absorption terms to ln (I_0/I_t). Actually, the measured μx is the absorption coefficient of everything between the two ionization chambers, including air, entrance and exit windows, etc. Furthermore, the sensitivities of the ionization chambers decrease with increasing x-ray energy, so there are a number of extraneous factors that multiply the ratio I_0/It. When the logarithm is taken, these multiplicative factors are transformed into a slowly varying additive background, which is easily subtracted out in the background subtraction. The extraneous materials in the beam path are not of concern, as long as they do not contain the elements being measured and they do not attenuate the beam very much.

As we have said, our method of determining the edge step is to fit first the data from a hundred eV or so below the edge using a linear function and also to fit the full range of data above the edge with low order polynomials (linear or quadratic), and then extrapolate them to the edge. In the case of EXELFS, a higher order polynomial (5^{th}) was necessary to fit the curvature of the rapidly decreasing post-edge spectrum. The difference between the pre-edge and post-edge fits extrapolated to the edge energy is the edge step, and is normalized to 1.

Caution: one should not use an edge feature, such as the highest peak in the spectrum, as a measure of the edge jump, because such XANES features are strongly dependent on the environment of the absorbing atom, and are therefore unreliable indicators of the total amount of the absorbing atom present in the sample. The fitting method described above puts little emphasis on the XANES region which is quite variable and therefore unreliable for normalization purposes, and compensates for trends in the background.

4.2.2 Choice of E_0

To convert to k-space, the value of E_0, the threshold energy must be specified. Fortunately the precise value is immaterial as long as it is within a rydberg (13.6 eV) or so of the edge, and that it is consistent for standard and unknown.

Physically, it makes more sense to choose E_0 somewhere near the bottom of the edge, close to the Fermi level. Since only relative shifts in E_0 between standard

and unknown are important, it does not matter whether the half-maximum point on the edge, or the bottom of the edge, or the top, is taken.

Relative E_0 shifts primarily affect the data at low values of k, which are distinguishable from changes in other structural parameters. Thus. ambiguities in absolute E_0 position, and small (< 3 eV) differences in relative E_0 position, do not introduce corresponding ambiguities in structure, determination by EXAFS. The choice of E_0 does pose significant uncertainties for k-space analysis in the XANES region, however.

4.2.3 Conversion to k-space

To be rigorous, conversion to k-space should be done before background subtraction so that the background fit does not preferentially follow the data at high energy (which oscillate slowly in energy space). This can be addressed ahead of time by collecting the experimental data on an even grid in k-space (which is possible with most data acquisition softwares), and therefore interpolation is performed when the change of variable is made. In any case, this turns out not to be an important issue in the end. A uniform grid in k- space is desirable so that standard discrete Fourier transform algorithms can be used. The sampling frequency must be high enough that the shortest wavelength in the data is sampled twice in a period, otherwise a rapid oscillation in the data may be confused with an oscillation at half the frequency. We have used a grid in k-space of $<0.05\ A^{-1}$, which is within standards.

5 Atomic Structure

In this chapter we examine the atomic structure of the Pd-Ni-P system from a semi-quantitative approach. We observe the atomic structure around all the constituent elements in $Pd_{30}Ni_{50}P_{20}$, $Pd_{40}Ni_{40}P_{20}$, and the $P_{60}Ni_{20}P_{20}$ BMGs, in the corresponding crystals for some cases, and in the alloys near the binary compositional ends.

The parameters that are of consequence in a qualitative discussion of the EXAFS and EXELFS results are: a) the distance and type of nearest neighbor, b) the coordination number of atoms at that distance, and c) the mean-squared displacement for a specific neighbor distance.

The position of the peaks can be affected by the phase shift, but for the Pd and Ni distances, we have calculated the phase functions for the nearest neighbors to be nearly the same for the Pd_3P and the Ni_3P model structures. The last of these is difficult to estimate if the entire peak of at that particular distance is not well resolved. The beat frequency for a peak splitting of ΔR is given by $k=\pi/(2\Delta R)$ and the resolution, so the resolution limit is $\Delta R>=\pi/(2k_{max})$, where k_{max} is the end of the k-range used. The mean-squared displacement can be obtained from a least squared fit (as you will find for the Pd_3P structure in Appendix A), but for that a model of the structure is required. Finally, the scattering amplitudes are different for the different elements, and this can lead to confusion as peak amplitudes are compared across a composition series. Please refer to the analysis of the Pd EXAFS as the interpretive

methodology to be used for the analysis of the local environments around Ni and P, to follow.

5.1 Local Structure Around Pd: Compositional Trends

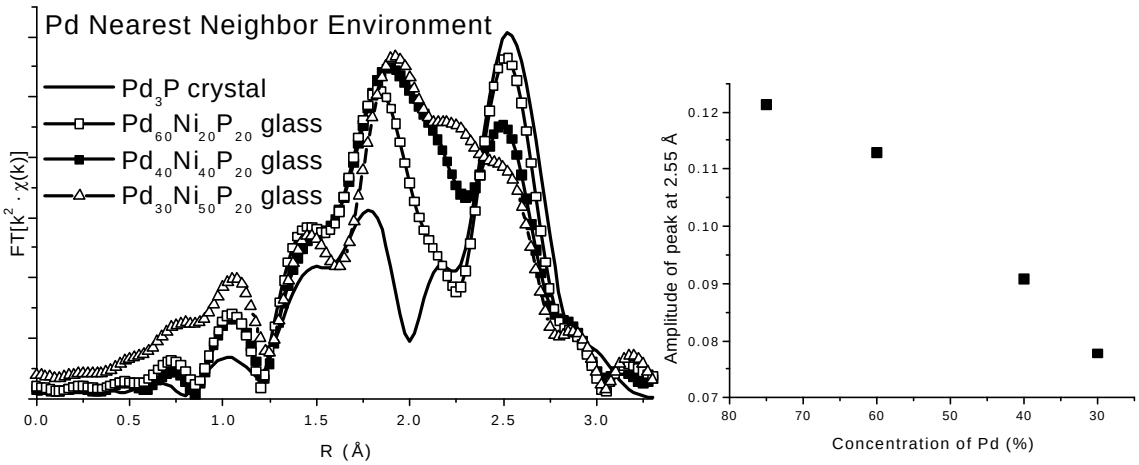

Figure 5-1: a) Comparison between the Pd nearest neighbors in the alloy system, and b) the amplitude of the peak at ~2.5 Å as a function of Pd concentration.

In Figure 5-1a we have the comparison between the Pd FT[$k^2 * \chi(k)$] of three ternary BMG alloys as well for the Pd_3P crystal. We observe a continuous change in structure as a function of increasing Pd concentration. The nearest neighbor (nn) environments of Pd in $(Pd\text{-}Ni)_{80}P_{20}$ glasses and the Pd_3P crystal are shown in Figure 5-1. We can clearly see two distinct nearest neighbor environments, from 0.9 – 2 Å and from 2 - 3 Å in the Pd_3P crystal, keeping in mind that these distances are not absolute, since amplitude and phase shift corrections have not been made for this structure. These two regions, in fact, delineate the two sets of nearest neighbor distances around a Pd atom, the Pd-P and Pd-Pd distances which are separated by an average distance

of about 0.7 Å. Since we used information out to k=14.4 $Å^{-1}$ for the Fourier transform displayed in Figure 5.1a, we are able to observe any splitting ΔR greater

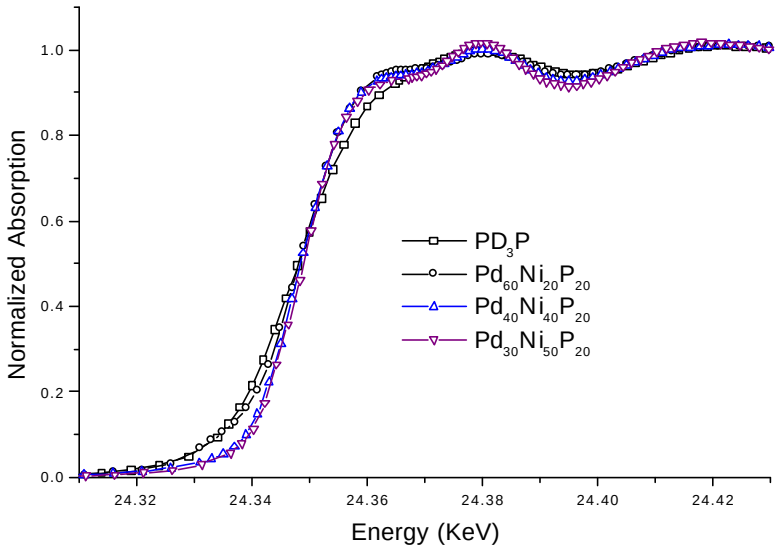

Figure 5-2: Comparison between Pd XANES in the alloy system.

than π/(2 x 14.4) = 0.109 Å. This is why we are able to see the separation of the Pd-P, Pd-Pd peaks in Pd_3P, where the difference in average nearest neighbor distance is (2.931-2.485)=0.446 Å [25].

We see that with the addition of Ni at the intermediate distances (between Pd-P and Pd-Pd distances) the peak at ~ 1.85 Å becomes less resolved, while at the same time we begin to see the peak at the intermediate distance of about 2.2 Å (which we may attribute to a Pd-Ni distance) increase in amplitude and thereby become better resolved.

The increase in amplitude of the peak attributed to the Pd-P distance (~ 1.8 Å) is large as one goes from Pd_3P to $Pd_{60}Ni_{20}P_{20}$ considering that only about 20% of Ni has been intruduced into the structure. Further, the peak loses intensity in approximately the ratio of the concentration of Pd (Figure 5-1b). A similar, and opposite effect takes place at 2.2 Å, where we may assume that Ni is being introduced to the structure. If the peak at 2.2 Å is due to the Ni neighbors of Pd, then we observe a continuous substitution of Ni for Pd as we go from Pd_3P to $Pd_{60}Ni_{20}P_{20}$.

The same is not true for the Pd-P peak at ~ 1.85 Å. Here we see that with the addition of Ni, as we go from Pd_3P to $Pd_{60}Ni_{20}P_{20}$, and then further to alloys with higher concentrations of Ni, we do not observe any significant change in the amplitude. So, the peaks at the two distances are not changing in a concerted way as a function of composition. Is it, then, possible to still consider the Pd_3P crystal as the structural motif for these glasses?

To answer this question, we look at the near-edge structure of the Pd edge in this series. For a selection rule allowed transition, as in the case of the K-edge, the near-edge structure in an X-ray absorption spectrum can be approximated by the density of states weighted by the transition matrix element. In Figure 5-2 we observe the change in the local density of states in the conduction band at the Pd sites. We see that this change is continuous, suggesting that the chemical environment around Pd in the glasses is similar to that of Pd_3P with a continuous modification electronic structure as Ni is incorporated into the glass structure.

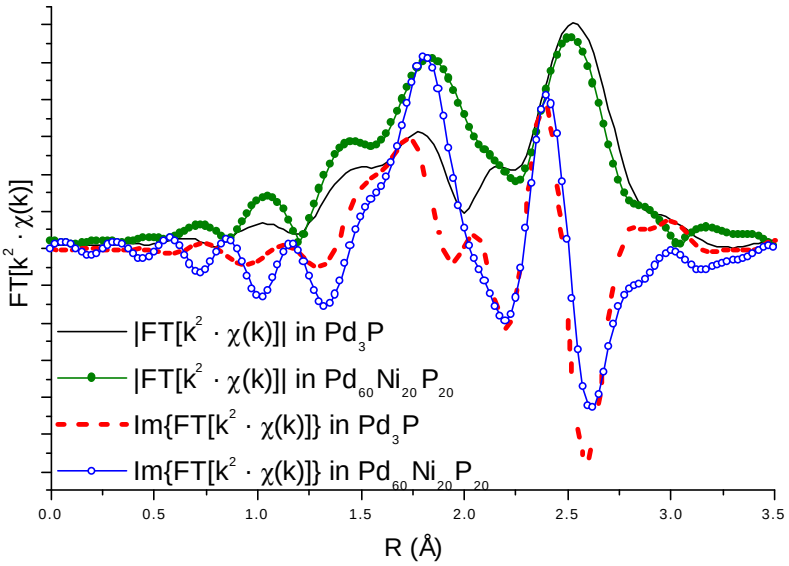

Figure 5-3: The modulus and the imaginary part of FT[chi(k)] in $Pd_{60}Ni_{20}P_{20}$ and Pd_3P

Once again, it is imperative that we not forget that the amplitude of a peak in |FT[k^2· ÷(k)]| is proportional to the coordination number but is also proportional to other functions that may have an influence. It is possible that the tails of the Pd-Ni scattering paths in the region of the Pd-P paths provide the excess amplitude. Without a rigorous fit of the experimental spectrum to a model one, we cannot be very certain of this. The problem is that we do not yet have a model in which we have enough confidence!

All is not lost, however. We have at our disposal the imaginary part of the FT[k^2· ÷(k)], which gives us the phase information from the scattered electrons. The difference in the peak positions of |FT[k^n· ÷(k)]| and Im{FT[k^n· ÷(k)]} (henceforth referred to as |FT| and Im{FT}, respectively) can be defined as δ. This δ parameter is

related to the chemical environment of the excited atom as well as that of the scatterer [41]. If we compare the imaginary parts and the magnitudes of the Fourier transforms of the $[k^2 \cdot \chi(k)]$ functions for Pd_3P and $Pd_{60}Ni_{20}P_{20}$, we should get further clues as to the types of nearest neighbors of Pd in the two cases through changes in δ.

We observe in Figure 5-3 that the Im{FT} functions line up very well in the region of 2.2-2.8 Å where the Pd-Pd bonds occur. More importantly, the δ for the two alloys in this region appears to be the same. This tells us that the type of scatterer at this distance does not change upon the introduction of Ni into the system.

An inspection of the region of the Pd-P bond, 1.7-1.9 Å, reveals that the δ does not change for this nearest neighbor. Therefore, the incorporation of Ni into a Pd_3P-like structure in order to obtain $Pd_{60}Ni_{20}P_{20}$, does not involve a change in the nearest

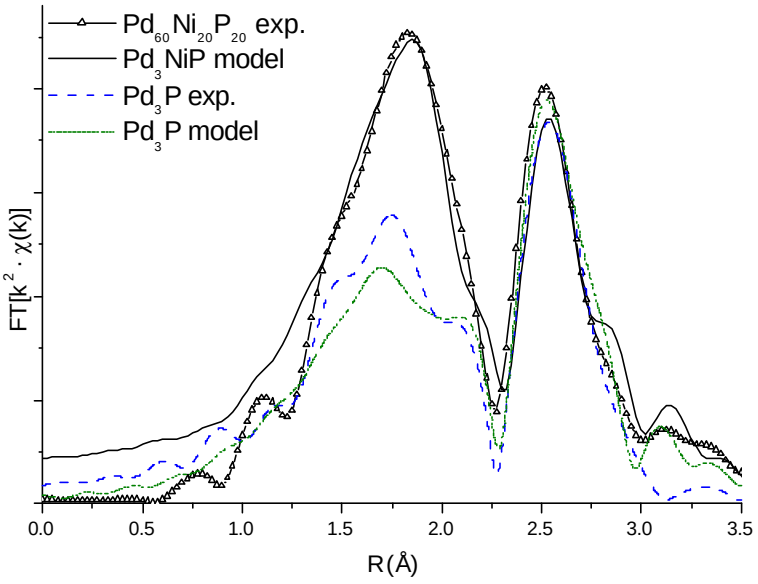

Figure 5-4: The fitting of the Pd_3P and the $Pd_{60}Ni_{20}P_{20}$ alloys with model structures based on the Pd_3P motif.

neighbor environment of Pd.

In the region of 2.0-2.25 Å, however, we do begin to observe some changes occurring. The Im{FT} function for Pd_3P goes through a minimum and a maximum while that for $Pd_{60}Ni_{20}P_{20}$ does not. This tells us that there is a significant change occurring in the type of scatterer at the intermediate distances, which does not have any impact on the higher bond distances (Pd-Pd bonds) but leaves a scattering contribution at lowest bond distances (Pd-P bonds). The Pd nn environment in $Pd_{60}Ni_{20}P_{20}$, therefore, resembles a modified Pd_3P structure, with new atomic neighbors (most likely Pd-Ni) at distances between Pd-P and Pd-Pd ones. The peak due to these new atomic neighbors increases in amplitude with increasing Ni content (at the expense of Pd neighbors) and at distances in between Pd-P and Pd-Pd bonds.

We are now in a position to attempt to model the theoretical EXAFS for the $Pd_{60}Ni_{20}P_{20}$ structure using the Pd_3P motif. The following is a scheme for First an 8 Å cluster of Pd_3P was created using its crystal structure. Next, the theoretical scattering amplitude and phase functions for each of the scattering paths of the photoelectron were calculated using the FEFF 7 [42] program. Since Pd_3P has two non-equivalent Pd sites at each Bravais lattice point, two separate cluster calculations had to be performed, one for each of the two Pd absorbers. The model functions were fit to the experimental through a least-squares analysis. In doing so, the weighted contributions of each of the two Pd sites were used. The details of the best fit of model Pd_3P to experimental Pd K-edge data are given in Appendix A.

The $Pd_{60}Ni_{20}P_{20}$ alloy was simulated by substituting some of the Pd-Pd distances with Pd-Ni ones to attain a stoichiometry of Pd_3NiP. As in the case of Pd_3P, the fit used the weighted contributions of the two non-equivalent Pd sites. In Figure 5-4 we see the comparison between the experimental and model (from FEFF 7) |FT| plots for Pd_3P and $Pd_{60}Ni_{20}P_{20}$ alloys. We can see that the region of Pd-P, Pd-Ni and Pd-Pd neighbors is very well accommodated by the Pd_3P crystal with its the necessary Ni substitution.

Taking this analysis further to now include all three bulk glass compositions, we see that in Figure 5-5 a discontinuity occurs in the region of the first peak, as we move from the $Pd_{60}Ni_{20}P_{20}$ to the $Pd_{40}Ni_{40}P_{20}$ glass. At this position, the δ parameter for $Pd_{60}Ni_{20}P_{20}$ glass is not the same as that for $Pd_{40}Ni_{40}P_{20}$. Going from $Pd_{40}Ni_{40}P_{20}$

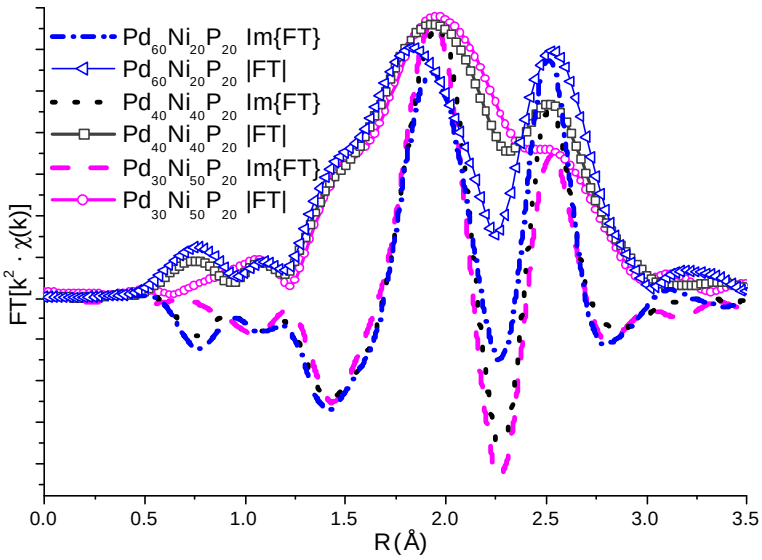

Figure 5-5: The modulus and the imaginary part of FT[chi(k)] in $Pd_{60}Ni_{20}P_{20}$, $Pd_{40}Ni_{40}P_{20}$ and $Pd_{30}Ni_{50}P_{20}$ from Pd EXAFS.

to $Pd_{30}Ni_{50}P_{20}$ in the same region, we observe that there is no change in δ. This implies that there is a change in the type of the average scatterer at the Pd-P distance as we go from $Pd_{60}Ni_{20}P_{20}$ to $Pd_{40}Ni_{40}P_{20}$, but the same is not true in the change from $Pd_{40}Ni_{40}P_{20}$ to $Pd_{30}Ni_{50}P_{20}$.

If we believe that the structure around Pd in the three glasses are a part of a continuous series, then the |FT| function for $Pd_{40}Ni_{40}P_{20}$ should be a linear combination of those from $Pd_{30}Ni_{50}P_{20}$. In Figure 5-6, we observe that the match between the simulated spectrum and the actual |FT| functions is particularly good in the region of the Pd-Pd distances, but there is a slight discrepancy between the width and distribution of the first major peak. This peak is too narrow in the simulated spectrum, suggesting an overestimation of the influence of the $Pd_{60}Ni_{20}P_{20}$ structure in

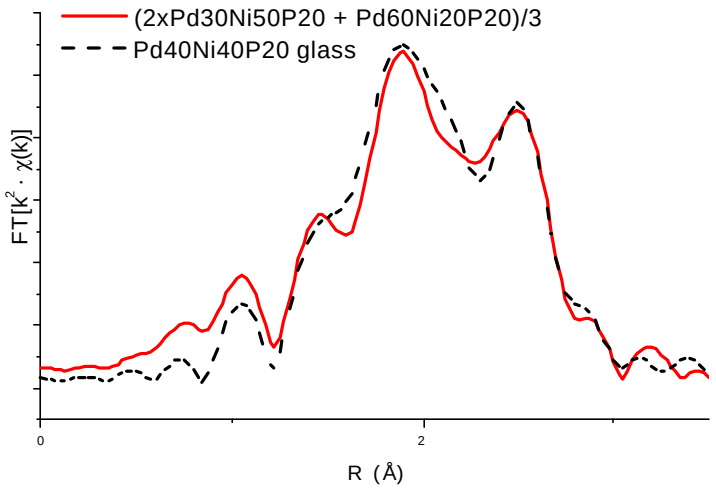

Figure 5-6: The simulated and actual |FT| for the $Pd_{40}Ni_{40}P_{20}$ glass.

this region. As we have seen in Figure 5-5, the Pd environment in $Pd_{40}Ni_{40}P_{20}$ follows the $Pd_{30}Ni_{50}P_{20}$ structure more closely.

The compositional trends in the structure around Pd can be summarized as follows:

1. The nearest neighbor distances in $Pd_{60}Ni_{20}P_{20}$ glass can be resolved into the Pd-P and Pd-Pd distances similarly to the Pd_3P crystal, with the exception that in the region where Pd-Ni distances are expected some additional peaks appear in the PRDF of the ternary glass. This accommodation, of the new Pd-Ni neighbors, can be modeled by a Pd_3NiP structure based on the Pd_3P structural motif.
2. The Pd local DOS in the conduction band is similar in the ternary glasses to that of Pd_3P with a continuous change as a function of composition.
3. In the region of Pd-P and Pd-Ni neighbors, the $Pd_{40}Ni_{40}P_{20}$ and the $Pd_{30}Ni_{50}P_{20}$ glasses are very similar to one another in the type and positions of these neighbors. In the same region, the neighbors of Pd in $Pd_{60}Ni_{20}P_{20}$ are, however, different in type.
4. In the region of Pd-Pd distances, the atom types and the positions in all three glasses are the same and follow the Pd_3P structure.

5.2 Local Structure Around Ni: Compositional Trends

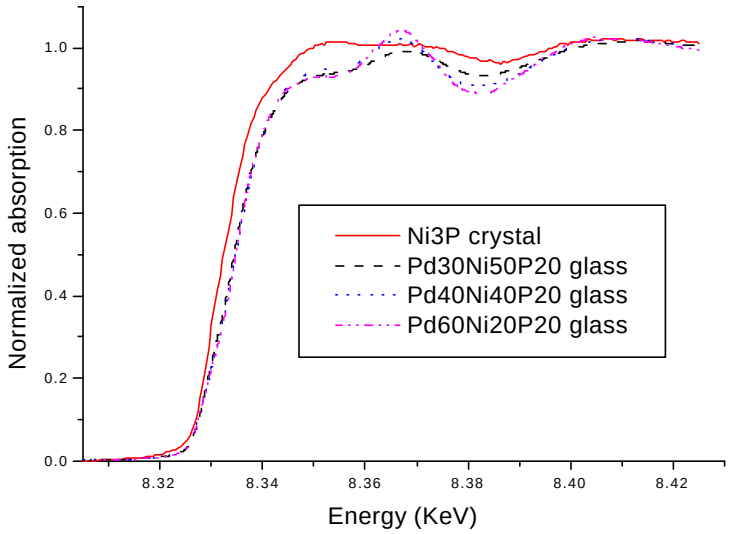

Figure 5-7: Comparison between Ni XANES in the alloy system.

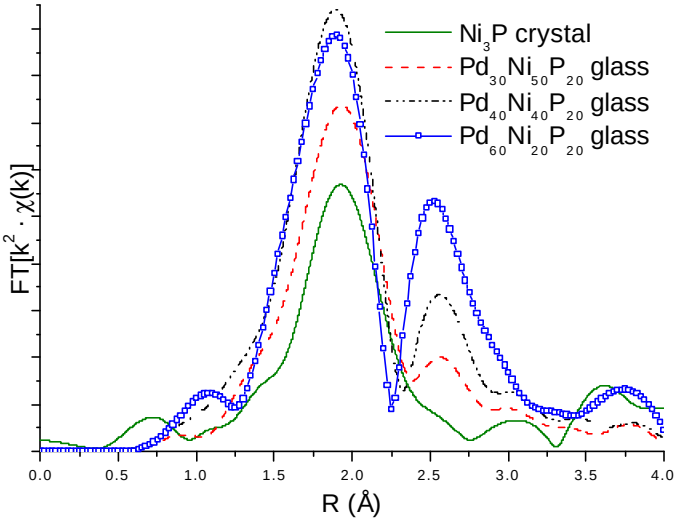

Figure 5-8: Comparison between the Ni nearest neighbors in the alloy system

We may begin the analysis of the local environment around Ni in the same manner as we have done for Pd. We will compare the ternary glassy alloys along with the binary Ni_3P in order to map the progression of the local atomic and electronic structure as a function of composition. In Figure 5-7 we see that the addition of Pd to the Ni_3P alloy to produce ternary alloys causes a discontinuous change in the conduction band electronic structure. Unlike local environment of Pd atoms, the chemical bonding around Ni in the ternary glasses does not show a continuous change from the environment around Ni in the binary Ni_3P crystal.

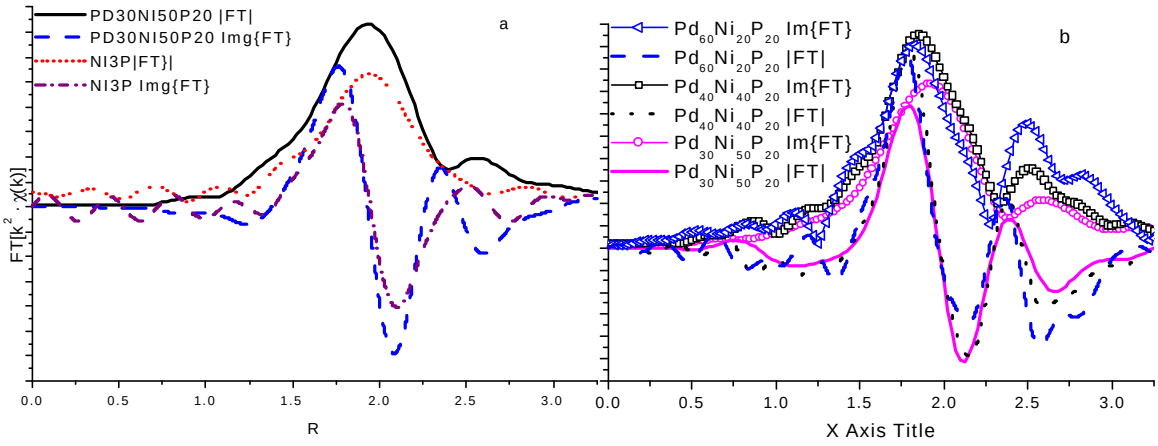

Figure 5-9: The |FT| and Im{FT} of a) Ni_3P and $Pd_{30}Ni_{50}P_{20}$ in $Pd_{60}Ni_{20}P_{20}$, and b) $Pd_{40}Ni_{40}P_{20}$ and $Pd_{30}Ni_{50}P_{20}$, from Ni EXAFS.

If we now look at the nearest neighbors of Ni we see a progression of peak intensities in the region of Ni-Pd distances in |FT| (Figure 5-8) as we had around the Pd environment (Figure 5-1a). As the Ni concentration increases, the peak corresponding to the Pd neighbor decreases. However, the peak at the shorter distance

(at ~ 1.8 Å) first increases and then appears to decrease again in amplitude as a function of increasing Pd concentration. The discontinuity in amplitude occurs at $Pd_{40}Ni_{40}P_{20}$ as a function of Ni concentration. The decrease in amplitude in this first peak as we go from $Pd_{40}Ni_{40}P_{20}$ to $Pd_{60}Ni_{20}P_{20}$ may or may not be real. For now, we can say that in this coordination shell, these two glasses seem isostructural.

We may continue, in analogy with our examination of the Pd environment, by asking whether or not $Pd_{30}Ni_{50}P_{20}$, the BMG composition with the highest concentration of Ni is isostructural with Ni_3P. The phase information once again provides us with the answer to this. In figure 5-9a we see that, indeed, the δ parameter does not change as Pd is incorporated into $Ni_{80}P_{20}$ to attain $Pd_{30}Ni_{50}P_{20}$. However, in Figure 5-9b*, we observe a change in δ in the first coordination shell, as we substitute some Ni atoms for Pd ones to go from $Pd_{30}Ni_{50}P_{20}$ to $Pd_{40}Ni_{40}P_{20}$. The change from $Pd_{40}Ni_{40}P_{20}$ to $Pd_{60}Ni_{20}P_{20}$, again, is *not* accompanied by a change in δ.

* The careful reader will have noticed that the plots of |FT| for the ternary glasses in Figure 4.8b are not identical to those in Figure 4.7. This is simply a result of a fact that the k-range of the data available to the author for Ni_3P is more limited than those for the ternaries and so in the first plot, for accurate comparison, Fourier transform was taken over this limited range for all the data. This restriction was lifted for the ternaries in the later plot so that more detail could be revealed.

For the sake of completion we should look at a comparison between |FT| of $Pd_{40}Ni_{40}P_{20}$ and a weighted average of the $Pd_{30}Ni_{50}P_{20}$ and $Pd_{60}Ni_{20}P_{20}$, as we had done for the Pd environment. In Figure 5-10, we see that the match is good for the Ni-Ni and Ni-Pd distances, but the amplitude is underestimated by the simulated plot in the region of the first peak where Ni-P distances should occur. The $Pd_{40}Ni_{40}P_{20}$ glass is closer to the $Pd_{60}Ni_{20}P_{20}$ glass in this region, as we have already seen from the phase

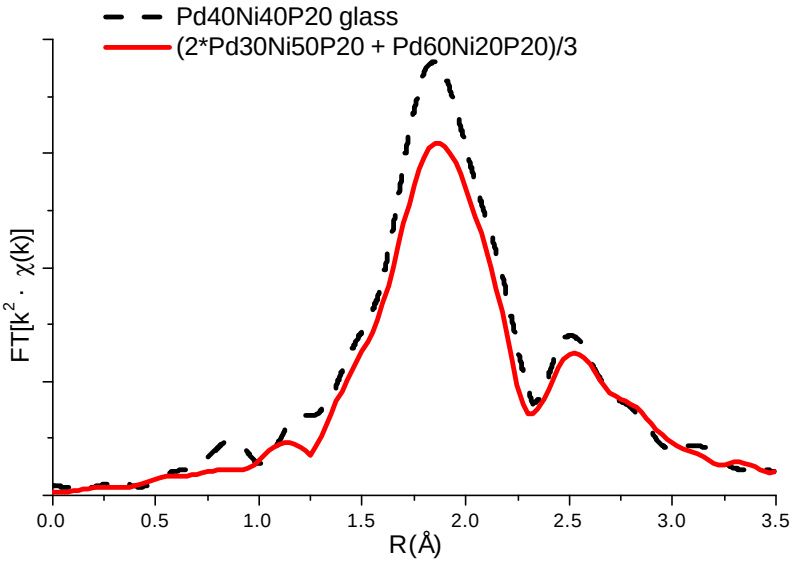

Figure 5-10: The simulated and actual |FT| for the $Pd_{40}Ni_{40}P_{20}$ glass.

information. Therefore, while the $Pd_{30}Ni_{50}P_{20}$ glass is isostructural to the Ni_3P crystal, the $Pd_{40}Ni_{40}P_{20}$ glass is isostructural to the $Pd_{60}Ni_{20}P_{20}$ glass.

We can summarize the compositional trends of the Ni nearest neighbors in the following way:

1. The Ni local DOS in the conduction band of the ternary glasses are different from that of Ni_3P, while the change within the alloys is continuous.
2. The $Pd_{30}Ni_{50}P_{20}$ glass is isostructural with the Ni_3P crystal, while $Pd_{40}Ni_{40}P_{20}$ and $Pd_{60}Ni_{20}P_{20}$ glasses are similar to the $Pd_{30}Ni_{50}P_{20}$ glass only at the Ni-Pd distance.
3. The $Pd_{40}Ni_{40}P_{20}$ and $Pd_{60}Ni_{20}P_{20}$ glasses are isostructural.

5.3 Local Structure Around P: Compositional Trends

We finally come to the local environment around P. So far, we have discovered that there are at least two types of structural units, based on the Pd_3P and the Ni_3P motifs, that exist in the $Pd_xNi_{(80-x)}P_{20}$ glasses. It is perhaps best to examine the structural changes in this composition range from the perspective of the P atom since it is the only element whose concentration is fixed across this range.

In Figure 5-11a we see that the first main peak in |FT| moves to larger distances as a function of increasing Pd concentration, as expected. At first glance, $Pd_{40}Ni_{40}P_{20}$ seems to follow the structure of $Pd_{30}Ni_{50}P_{20}$, albeit, with a slightly larger nearest neighbor distance. However, if we look in the same region in Figure 5-11b, we notice that the relative phase shift measured between the peak positions of |FT| and Im{FT} functions in $Pd_{40}Ni_{40}P_{20}$ glass is the same as that for the $Pd_{60}Ni_{20}P_{20}$ glass.

One important distinction can be drawn between the Im{FT} functions for the transition metal edges, versus that of P. If we look back at the Im{FT} functions for

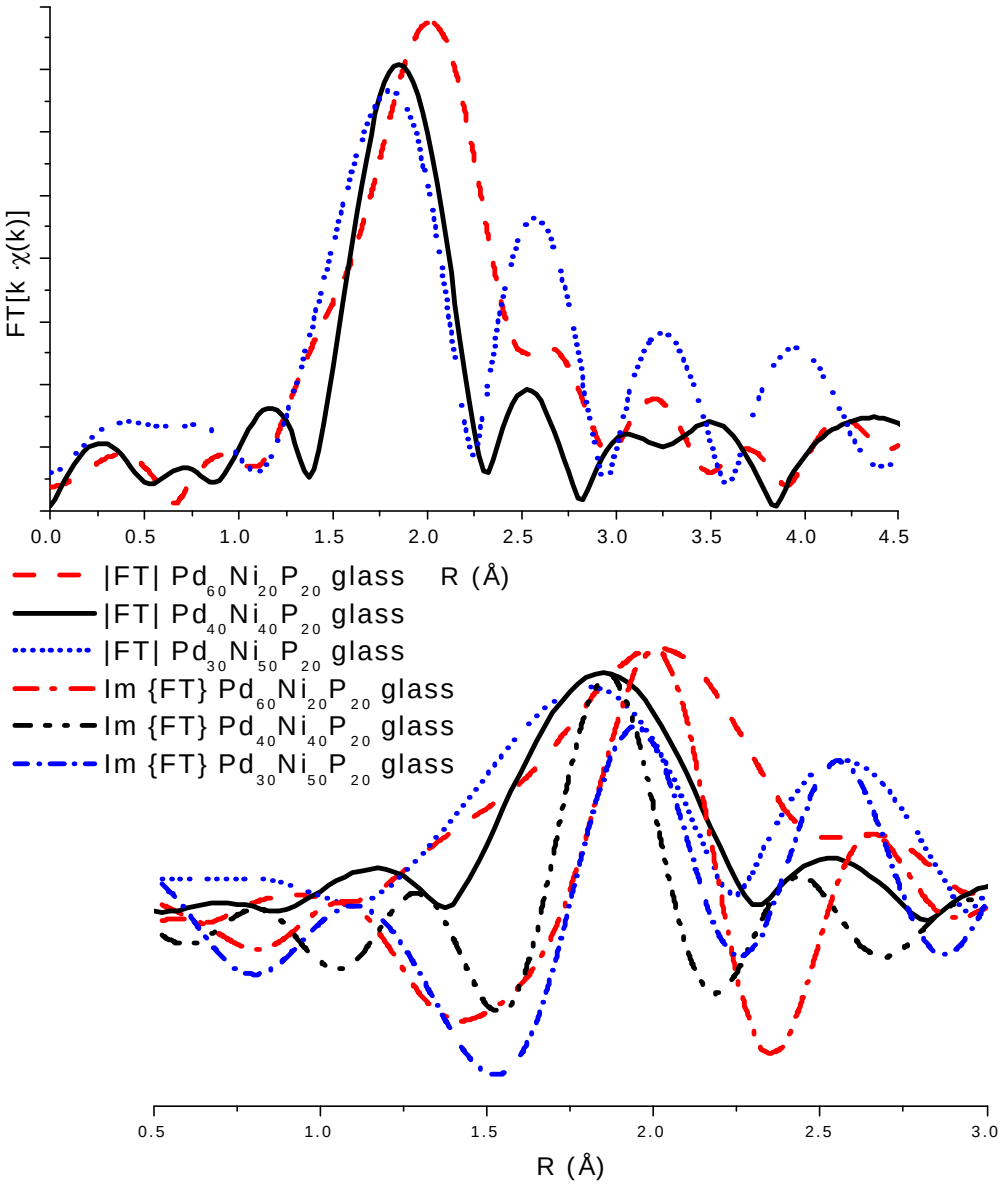

Figure 5-11: The |FT| (a) and the |FT| along with the Im{FT} (b) of the $Pd_{60}Ni_{20}P_{20}$ $Pd_{40}Ni_{40}P_{20}$ and $Pd_{30}Ni_{50}P_{20}$ glasses from P EXELFS.

the Pd and Ni edges of the ternary glasses, we notice that the tendency is for these functions to remain aligned across the composition series. That is, in the case of the electrons ionized from Pd and Ni, the potential field encountered by these electrons was nearly the same even as the average composition changed. This is not the case for the electrons ionized from P atom electrons. In Fig 5-11b we can clearly see that the Im{FT} does not remain aligned as a function of composition. The electronic structure around the transition metals is not very sensitive to the composition changes while that around P is. If, indeed, the Pd_3P and Ni_3P structures are found in the ternary glasses then, in either case, P sits inside a cage of 9 transition metals. P will most likely have chemical bonds with these metals due to the electronegativity difference between them and itself. Therefore, the environment around P will be highly sensitive to changes in chemical bonding, and so, as we move from the $Pd_{30}Ni_{50}P_{20}$ to the $Pd_{40}Ni_{40}P_{20}$ glass, the Im{FT} functions for the two cases do not remain in phase. We propose that being in phase would be a manifestation of the pseudo band-structure stabilization coming from an interference between the Fermi surface and the first peak in the structure factor. This stabilization governs the phase alignment for the environment of the transition metals, but it fails in the immediate neighborhood of P. We will explore this point further when we examine the electronic structure in these alloys.

The δ parameter remains nearly equal between the $Pd_{40}Ni_{40}P_{20}$ and the $Pd_{60}Ni_{20}P_{20}$ while being different for differs from that of $Pd_{30}Ni_{50}P_{20}$. This leads us to conclude that the P nearest neighbor environment around P in $Pd_{40}Ni_{40}P_{20}$ is similar to

that of $Pd_{60}Ni_{20}P_{20}$ (which has been ascribed a modified Pd_3P structure) but different from that of $Pd_{30}Ni_{50}P_{20}$ (which has been ascribed the Ni_3P structure).

5.4 Crystallization

We have observed the changes in the local atomic structure as a function of crystallization. In Figure 5-12 we show the change in local structure of the transition metals as a function of crystallization. Both the |FT| and the Im{FT} functions are plotted for each composition and for each transition metal.

We observe that the $Pd_{60}Ni_{20}P_{20}$ glass undergoes very little change in the local atomic configuration of both Ni and Pd. Ni-P distances ($r < 1.8$ Å) for this glass remain unchanged in both position and type, as we can ascertain from the Im{FT} and |FT| plots. The same is true for the Pd-P distances. As we move to the 2^{nd} and 3^{rd} peaks, we observe that upon crystallization, the Ni-Ni nearest neighbors increase at the expense of Ni-Pd ones, while the opposite happens for the Pd environment, where the Pd-Pd neighbors increase at the cost of Pd-Ni ones. We can say the following about the process of crystallization of the $Pd_{60}Ni_{20}P_{20}$ glass:

1. In the process of crystallization a phase separation takes place whereby Ni atoms have an increase in Ni neighbors while sacrificing some Pd ones, and vice versa for Pd environment. This change takes place with a minimum readjustment of the coordination environment around both the transition metals. No shifts in either Im{FT} or |FT| at the TM-P (TM = Ni,Pd) distances indicate that for this glass, crystallization does not require breaking of nearest neighbor bonds with P.

2. Upon crystallization, the TM-TM distances increase, as seen by shifts in Im{FT}. Since the density of this alloy increases slightly upon crystallization [43] (Figure 5-13), the increase of the Pd-Pd bond distance indicates that the Pd atoms are packing more efficiently upon crystallization. There is an increase in ordering for the Pd-Pd neighbors.

Compared to the case of $Pd_{60}Ni_{20}P_{20}$, the Ni neighborhood in the $Pd_{40}Ni_{40}P_{20}$ and the $Pd_{30}Ni_{50}P_{20}$ glasses undergo much more dramatic changes upon crystallization. The effect of crystallization on the Ni-P distances in these alloys is difficult to resolve from changes in the Ni-Ni distances. However, what can be said unambiguously is that, unlike what we observe for the $Pd_{60}Ni_{20}P_{20}$ alloy, there are increases in the amplitudes of both the Ni-Ni and the Ni-Pd neighbors in these two alloys. That is, even if the increase in the Ni-Ni nearest neighbor peak amplitude does occur at the expense of decreasing Ni-Pd neighbors, the peak amplitude in |FT| is offset by an increase in overall ordering.

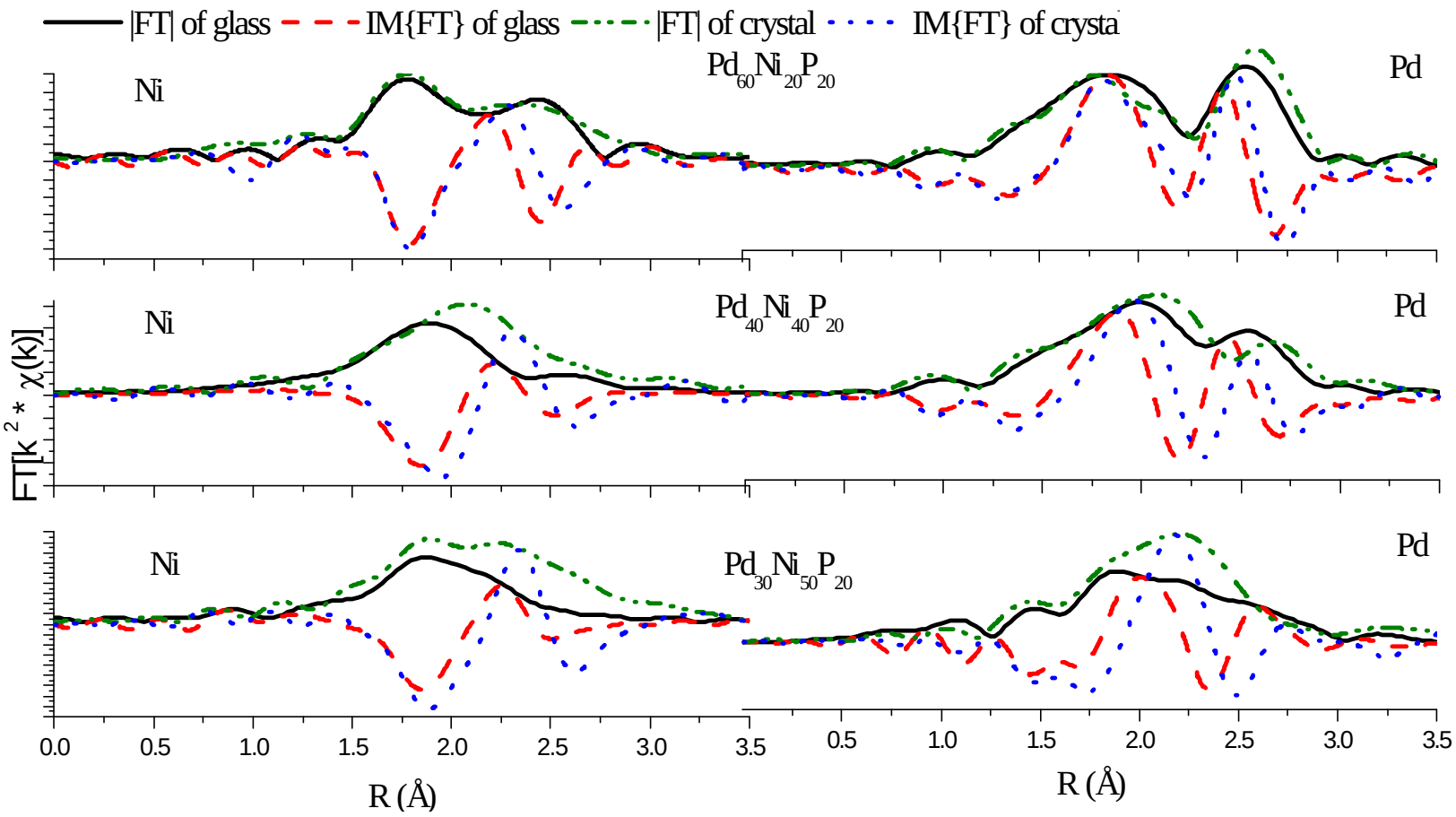

Figure 5-12: The |FT| and Im{FT} functions for the $Pd_{60}Ni_{20}P_{20}$, $Pd_{40}Ni_{40}P_{20}$ and the $Pd_{30}Ni_{50}P_{20}$ alloys in both the glassy and crystalline states.

Looking at the Ni and Pd environment for $Pd_{40}Ni_{40}P_{20}$ we see from a no discernable change in δ upon crystallization even with the significant shift in |FT| to larger distances, indicating that all the nearest neighbors of the TMs in this alloy move to slightly larger distances upon crystallization without a change in the type of nearest neighbor. The fact the bond distance increase upon crystallization, is consistent with the increase in the volume of this glass upon crystallization from the data of Chen et al., but is contentious with that from Harms and Schwarz [44]. Therefore, it is difficult to say, in this case, whether the increase in the bond distance is associated with an overall lattice expansion or an increase in ordering. However, the increase in

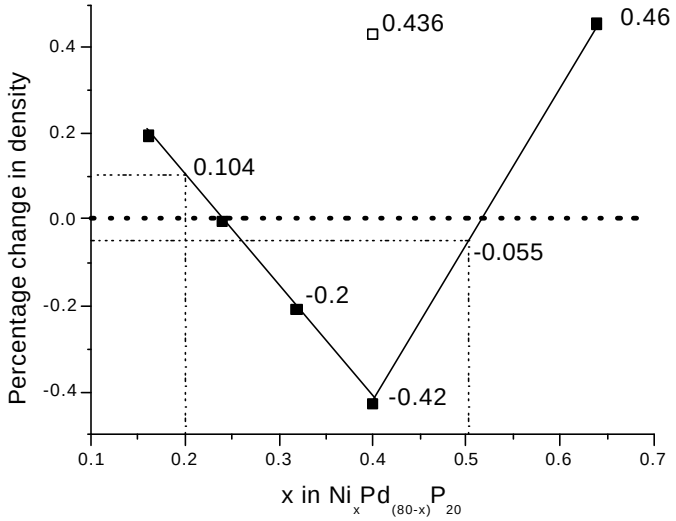

Figure 5-13: Density changes as a function of crystallization of the $NixPd_{(80-x)}P_{20}$ glass as reported by Chen et al. [43], showing negative density changes for the $Pd_{40}Ni_{40}P_{20}$ and the $Pd_{30}Ni_{50}P_{20}$ (interpolated) alloys! The density change is positive for the $Pd_{60}Ni_{20}P_{20}$ alloy. Harms and Schwarz have also measured the density change for the $Pd_{40}Ni_{40}P_{20}$ glass and report a density increase (shown as ð in the figure) for this alloy upon crystallization [44].

amplitude of the |FT| function for Ni at the Ni-TM neighbors is not offset by a corresponding decrease in amplitude for the Pd-TM, indicating that there is more than

just the readjustment of the TM-TM coordination. There must necessarily be an increase in ordering taking place at TM-TM distances in this alloy.

In the case of the $Pd_{30}Ni_{50}P_{20}$, the amplitude of the both the TM-P peaks are increasing with crystallization. However, the P concentration remains fixed during this transformation, and so the number of P neighbors cannot increase for both of the TMs. Therefore, it can be concluded that the increase in the amplitudes must necessarily include an increase in ordering of the TM-P bonds.

6 XPS Data

The following core level shifts were observed:

a. Pd $3d_{5/2}$ binding energies in the alloys are shifted *higher* by 0.87-0.97 eV in comparison to those of pure Pd obtained experimentally.

b. Ni $2p_{3/2}$ binding energy in the alloys are shifted *higher* by 0-0.16 eV in comparison to those of pure Ni. Ni binding energy in crystalline $Pd_{70}Ni_{10}P_{20}$ is the same as that for pure Ni. The binding energy for pure Ni was obtained experimentally.

c. P $2p_{1/2}$ and $2p_{3/2}$ binding energy in the alloys are shifted *lower* by 0.32-0.45 eV and 0.15-0.31 eV in comparison to those of pure P. The core levels for pure P was obtained from literature [45]

d. For glasses the shifts in binding energies with respect to those of the pure elements are constant in the case of Pd and Ni. The shifts for P, however, are similar to those in the crystals.

Table 6-1: The core-level energies of the glassy and crystalline alloys in the $Pd_xNi_{(80-x)}P_{20}$. The values of the elemental core levels are given as 'e'.

	Glassy			Crystalline		
	$Pd_{60}Ni_{20}P_{20}$	$Pd_{40}Ni_{40}P_{20}$	$Pd_{30}Ni_{50}P_{20}$	$Pd_{70}Ni_{10}P_{20}$	$Pd_{40}Ni_{40}P_{20}$	$Pd_{20}Ni_{60}P_{20}$
Ni ($2p_{3/2}$)/eV (e - 852.62)	852.75	852.74	852.75	852.62	852.70	852.78

Pd ($3d_{5/2}$)/eV (e – 335.05)	336.00	335.99	336.00	335.92	335.94	336.02
P ($2p_{3/2}$)/eV (e – 130.0)	129.84	129.74	129.69	129.85	129.77	129.72

The valence band and core-level XPS spectra of the $Pd_{40}Ni_{40}P_{20}$ are shown in Figure 6-1. The P and the Pd core-levels are exhibiting both the spin-orbit split

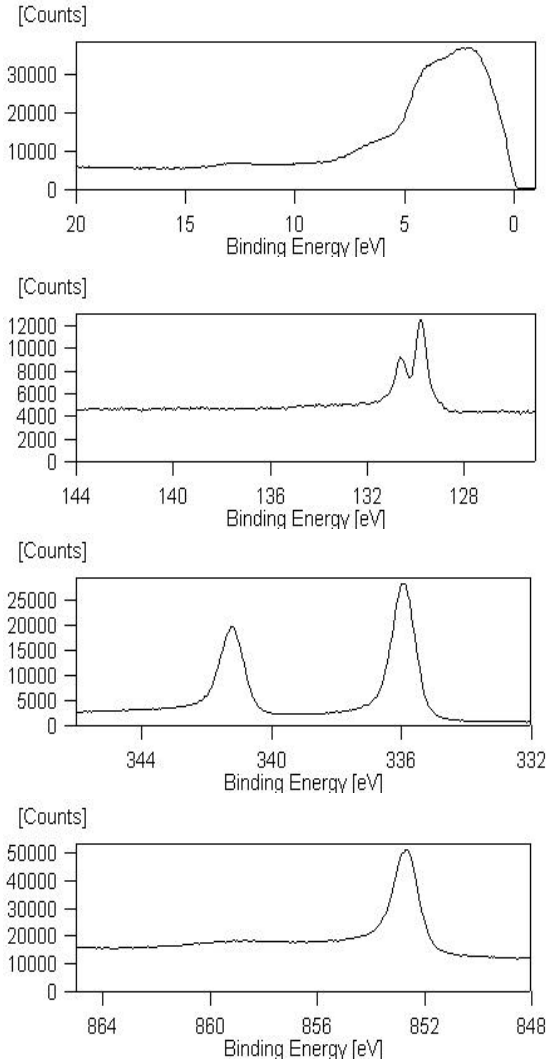

Figure 6-1. The P and the Pd core-level spin-orbit split peaks, and only the $2p_{3/2}$ peak for Ni. Spectra were obtained for the alloys in Table 6-1, $Ni_{80}P_{20}$ glass and the Pd_3P crystal.

peaks, whereas in Ni we show only the $2p_{3/2}$ peak. Similar spectra were obtained for all the alloys listed in Table 6-1, as well as the $Ni_{80}P_{20}$ glass and the Pd_3P crystal.

7 Stabilization of the Glass Structure

The stability of a glass system stems from its fundamental atomic and electronic structure. It is the result of a specific compositional mix of different atomic species at a given thermodynamic point. Its stability against crystallization depends on the relative stabilities of both the glass and crystal at particular thermodynamic point. The Pd-Ni-P BMGs, therefore, receive their stability from cumulative, and interrelated, effects of both atomic and electronic origin. We will explore the effect of packing (treating the atoms as non-interacting), the effect thermo-kinetic hindrances to crystallization (from our structural study of the crystallization), the effect of the electronic structure through the lowering of the electronic component of the free energy, and finally attempt to point out the interrelated nature of the atomic and the electronic effects of stabilization.

7.1 Atomic Structure Stabilization

7.1.1 Frustration

One important feature of the packing in 3-dimensional space by hard spheres is that of *frustration*. A ”frustrated” structure is one in which the particles in a ground state can not each assume the minimum free energy that is ideally available to each of them by virtue of interactions with only its nearest neighbors. Some of the particles are indeed at this minimum, but this necessarily forces others to be at a slightly higher

energy, or in structural terms, to have a lower packing density with their respective nearest neighbors. Therefore, there is a large degeneracy in the global ground state of the particle system.

How does this frustration come about? Is there not a 3-dimensional arrangement of hard spheres that can be attained starting from a liquid-like state that allows all the spheres to have the densest possible packing around them?

The densest possible packing of mono-sized spheres in two dimensions has an obvious non-degenerate solution. The equilateral triangular arrangement is the densest packing of 3 spheres. Adding another sphere creates a rhombus with one of its diagonals equal to the sides of the now two equilateral triangles. In this way all space can be filled resulting in densest possible arrangement in two dimensions.

How would this model translate to three-dimensional space? To simplify things, we will examine the features of the structure that are not sensitive to very local phenomena such as directional bonding and charge transfer between atoms. Also, for the sake of simplicity, we consider a static structure where the positions of atoms are fixed points in 3-dimensional space; i.e. thermal vibrations are ignored. We are therefore left with the structural issues of a dense random arrangement of atoms interacting with each other through an isotropic Lennard-Jones-like potential that is characterized by strong core-core repulsion and a weak long-range attraction.

Now if we try to carry the packing onto three dimensions under the energy minimization scheme lain out above, we see first of all that the densest way to pack 4 spheres is a regular tetrahedron. However, if we try to tile all 3-dimensional space

with regular tetrahedra, we run into pockets of empty space. Let us look at the example of placing regular tetrahedra around a bond and trying to come full circle. We can place 5 tetrahedra and then we are left with 7.4° of unfilled space. This space can be filled up if we allow the tetrahedra to be slightly irregular. Allowing the bond that is shared by the 5 tetrahedra to be 5% smaller than the other bonds in the tetrahedra the structure can swallow up the pocket. This results in a regular fivefold bipyramid. Now, if we can extend the fivefold bipyramid to all space then we will have, after all, the same environment around all the atoms, and we will have an unfrustrated structure. Placing 12 fivefold bipyramids around one of the axial atoms we end up with the icosahedron. Yet all of the *flat* 3-dimentional space cannot be filled by such icosahedra! This frustration of three-dimensional space leads to the stabilization of a dense randomly packed liquid against crystallization since there is be no stable crystalline phase as an alternative. An attempt to create a crystal would not be possible while still maintaining an overall tetrahedral close-packing. In order to form a crystal, therefore, some of the packing efficiency has to be sacrificed.

7.1.2 Modeling a Dense Randomly Packed System

Finney and Wallace [46] found in their molecular dynamics simulation of 999 particles that not a single particle had 12 fivefold bonds emerging from it; i.e. not a single icosahedron was found. The frustration of 3-dimensional packing further limits us in our use of fivefold bipyramids. Gaskell [47] argues that growing such structures, with a 7.4° angular mismatch, incorporates a cumulative strain and the structure

becomes ultimately self-limiting. When the elastic strain becomes large enough it becomes energetically preferable to nucleate a new structure.

The first physical simulation of the packing of hard spheres by long-range attractive forces was carried out in a set of groundbreaking experiments by Bernal [26]. He packed ball bearings into rubber bladders, kneaded them, and set them in black paint, to simulate the dense random packing of hard spheres (DRPHS). The positions of the balls then were individually determined methodically by hand and eye. This experiment initiated a host of similar simulations, with computers eventually taking over ball bearings and rubber bladders. In this DRPHS model Bernal found only five different canonical polyhedra with equal triangular faces, which were not large enough to allow another sphere of the same size inside them [Fig 7-1]. He found these polyhedra by examining the empty spaces defined by the nearest neighbor bonds. The relative concentration of each of these structures was found to exhibit a strong preference for tetrahedra (48% by volume), followed by octahedra (27% by

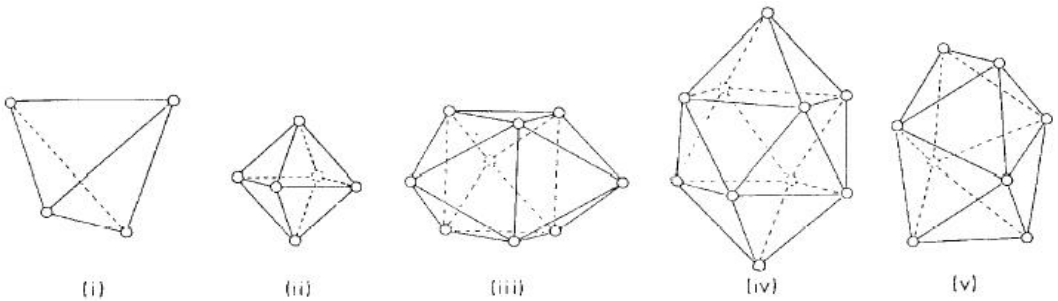

Figure 7-1: The Bernal holes showing the (i) tetrahedron, (ii) the octahedron, (iii) the trigonal prism, (iv) the tetragonal dodecahedron and (v) the Archmedian antiprism.

volume). The remaining volume was found to be occupied by the larger cavities; the tetragonal dodecahedra, the trigonal prisms and the Archemedian antiprisms occupying 15%, 8% and 2% of the volume respectively.

The results of Bernal's work were supported by a similar simulation study carried out by Finney [48] who developed a 7994 atom DRPHS model with a packing density $\eta = 0.6366 \pm 0.0004$.

It is with Finney's model that Cargill [49] compared his experimentally determined structure for amorphous $Ni_{76}P_{24}$. The fit was found to be very good considering that the comparison was between a model structure of densely packed spheres which have no interactions with one another except through surface contact and a real solid structure of *two different types of atoms* which are condensed to retain liquid-like disorder!

It will not be an exaggeration to say that the striking structural similarities between these early DRPHS models and Cargill's experiment revolutionized the existing concepts of the structure of metallic glass. An explanation for the success of the monoatomic DRPHS model with binary transition metal (TM) – metalloid (M) glass was given by Polk [50] who claimed that the three larger Bernal cavities from the DRP of TM atoms could be filled by the M atoms to attain the a-$TM_{80}M_{20}$ composition. It was later shown by others, that Polk's conjectures underestimated the size of the M atoms in fitting them into the *undistorted* cavities [47]. The trigonal prism, for example, of TM atoms with its cavity filled by an M atom remains undistorted only if the radius ratio of the M atom to the TM atom is less than 0.53.

For a-$Ni_{76}P_{24}$ it is ~ 0.72. If the radius ratio for Ni and P had been ~ 1, then by a simple geometrical argument, we would expect both Ni and P atoms to occupy the vertices of undistorted trigonal prisms. The larger cavities of the monoatomic DRPHS model are therefore ideal cavities, and it is safe to say that a densely packed system of two atoms whose radius ratios lie between 0.53 and 1.0 will try to distort those cavities somewhat while still retaining the denser tetrahedral and octahedral units.

So far the models we have considered have been constructed only on space filling criteria. No interatomic potentials have been used, no structural 'design' has been imposed on the model. Yet, even so we now already have some physical intuition into how structure of a TM-M metallic glass may be understood as a DRPHS. We have learned that: a) A set of 5 polyhedra can fill all space in a DRPHS model, and b) The proportions of tetrahedra to octahedra in a monoatomic DRPHS are followed quite impressively by a real metallic glass.

Glassy $Ni_{76}P_{24}$ is not unique in being essentially a DRPHS solid. Of course the DRPHS simulates very well monoatomic metallic glass but even for other TM-M glasses the model is just as applicable. For example the Fe-P, Co-P, Pd-Si and Pd-Ge glasses all show the tertrahedral-(split)octahedral features of the DRPHS model [47].

To pose a seminal question we may ask the following: How well does such a model structure for a dense, randomly packed, solid of equivalent atoms compare to an experimentally determined structure for a ternary metallic glass?

7.1.3 The structure of Pd-Ni-P

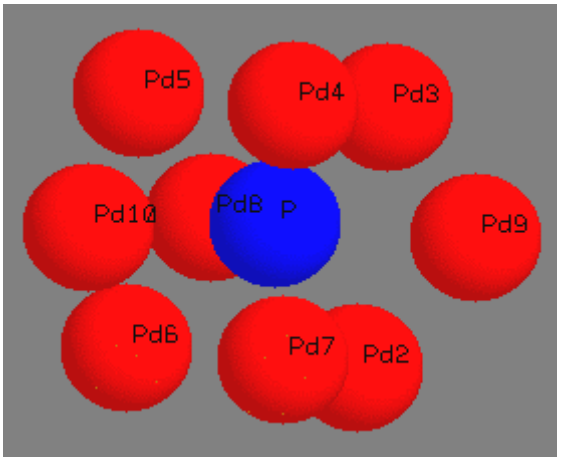

Figure 7-2: The trigonal prism is a naturally occurring structure in both Pd_3P and Ni_3P crystals. Here we see the Pd_3P structure where P sits in between two trigonal planes of Pd atoms and has three more Pd atoms laterally three half octahedral caps.

The applicability of Pd_3P and Ni_3P motif in describing the structure of $Pd_xNi_{(80-x)}P_{20}$ glass has been investigated and is discussed in Chapter 5.

We find the local structure around the Pd in $Pd_{60}Ni_{20}P_{20}$ glass can be resolved into the Pd-P and Pd-Pd distances similarly to the Pd_3P crystal, with the exception that in the region where Pd-Ni distances are expected some additional peaks appear ternary glass. This accommodation, of the new Pd-Ni neighbors, can be modeled by a Pd_3NiP structure based on the Pd_3P structural motif.

We find that he $Pd_{30}Ni_{50}P_{20}$ glass is isostructural with the Ni_3P crystal, and that from the perspective of the Ni atoms, the $Pd_{40}Ni_{40}P_{20}$ and the $Pd_{30}Ni_{50}P_{20}$ glasses are nearly isostructural. On the other hand, from the perspective of the Pd atom, $Pd_{60}Ni_{20}P_{20}$ glass is isostructural to Pd_3P while $Pd_{40}Ni_{40}P_{20}$ and $Pd_{30}Ni_{50}P_{20}$ are nearly

isostructural. In other words, Ni_3P and Pd_3P are structural motifs that can be combined to describe the structure of the whole BMG-forming range of $Pd_xNi_{(80-x)}P_{20}$.

It stands, therefore, that the Pd_3P and the Ni_3P structural motifs are indeed suitable for describing the local environments around Pd and Ni, respectively, in ternary Pd-Ni-P glass. Figure 7-2 shows the P environment of the Pd_3P structure. One can see that the Pd2-Pd7 atoms form a trigonal prism, where Pd3-Pd4-Pd5 forms one face and Pd2-Pd6-Pd7 forms the other. This prism is capped by the equatorially by the Pd8, Pd9 and Pd10 atoms. The capped trigonal prism is one of the canonical holes that Bernal had found in his analysis of the DRPHS model (see 7.1.2). This structure occurs naturally in both the Pd_3P and Ni_3P structures and, by extension, in the Pd-Ni-P glasses. This tells us that the densely packed structure of the glass is stabilized by the fact that alternative crystalline phases are themselves not very stable due to frustration of three-dimensional space.

Since P sits inthe middle of 6 transitional metal atoms (TM-P cluster) one can imagine the P to be at the center of an octahedral hole. In such a case, the average length of the bonds on the triangular faces (Pd3-Pd4-Pd5 and Pd2-Pd6-Pd7 in Fig. 7-2) should be close to the average length of the bonds forming the columns of the prism (Pd5-Pd6, Pd4-Pd7 and Pd3-Pd2 in Fig. 7-2). As the structure of this cluster approaches that of an octahedron, the ratio of average bond-lengths on the columnar faces (C_{avg}) to those of the triangular faces (T_{avg}) will approach 1. The C_{avg}/T_{avg} ratio for the P nearest neighbors in Pd_3P and Ni_3P crystals are tabulated in Table 7-1.

Table 7-1: The lengths of the bonds on the triangular faces, their average (T_{avg}), and similarly for the columnar faces, their average (C_{avg}), and the ratio of C_{avg}/T_{avg}.

	Triangle1			Triangle2			T_{avg}	Column			C_{avg}	C_{avg}/T_{avg}
Ni_3P	2.483	2.968	2.969	2.7608	2.709	2.577	2.859	2.903	3.394	3.484	3.26	1.181
Pd_3P	2.926	2.776	2.926	3.212	2.776	3.212	2.971	3.101	3.217	3.101	3.14	1.057

As we see, the C_{avg}/T_{avg} for Pd_3P is closer to 1 than that for Ni_3P. Since the ratio of atomic sizes of Pd to P is larger than that of Ni to P, it makes sense that a near-octahedral cluster of Pd atoms can accommodate a P atom in its center whereas a similar cluster of Ni atoms need to be distorted further away from an octahedron for a similar accommodation.

We further observe in Table 7-1 that the P nearest neighbor environment in Ni_3P is more disordered than that of Pd_3P. This is evidenced by the 5 non-equivalent bond distances seen on the triangular faces of the former versus the 3 seen in the latter. This difference is also seen in the columnar bonds. This higher ordering in the P nearest neighbors in Pd_3P compared to those of Ni_3P occurs in spite of the fact that the Pd_3P is a lower symmetry crystal than Ni_3P. This is an evidence of stronger Pd-P chemical interactions than Ni-P ones. The idea of dense random packing of *hard* spheres is therefore less applicable to Pd_3P and, by extension, $Pd_{60}Ni_{20}P_{20}$ glass than it is to Ni_3P and $Pd_{30}Ni_{50}P_{20}$ glass.

7.2 Thermo--kinetic Stability Against Crystallization

In general, a small change in the local structure indicates that the glass and the crystal have nearly identical local units, but differ only in the long-range arrangement of them. Typically in these situations, the driving force for the nucleation of a crystal from the glassy matrix is low. On the other hand, a large change in structure, especially beyond the first coordination shell indicates a large kinetic component to crystallization. From a thermodynamic point of view, if the Gibbs free energy difference $\Delta G_x(T)$ between the liquid and the available crystalline phases is low, then the glass-forming ability should be high. In terms of the changes in enthalpy, ΔH_x, and entropy, ΔS_x, upon crystallization from the glassy (pseudo-liquid) phase,

$$\Delta G_x = \Delta H_x - T\Delta S_x \qquad [7.1]$$

If the glassy and crystalline structures are nearly similar, then ΔH of transformation between the two should be small. This is the case for $Pd_{60}Ni_{20}P_{20}$.

A large positive ΔS_x will also reduce the thermodynamic incentive for crystallization. This is what we observe for the $Pd_{40}Ni_{40}P_{20}$ and the $Pd_{30}Ni_{50}P_{20}$ glasses.

The homogeneous nucleation and growth rates, (I) and (U) for a nucleus with a spherical morphology have been expressed as [51]:

$$I = \frac{10^{30}}{h} \cdot e^{\left[-16\pi a^3 b \,/\, 3(T_r(1-T_r)) \right]} \qquad [7.2]$$

and

$$U = \frac{10^2 f}{h} \cdot \left[1 - e^{\left\{ -b\Delta T_r \middle/ T_r (T_m) \right\}} \right] \quad [7.3]$$

where T_r is the reduced temperature(T/T_m), ΔT_r is the difference in temperature from T_m, η is the viscosity, *f* is the fraction of the nucleation sites which are present at the growth interface, and α and β are related to σ, the liquid/solid (in this case, glass/solid) interface energy, and to ΔH_x and S_x given by, $\alpha=(NV)^{1/3}\sigma/\Delta H_x$ and $\beta= \Delta S_x/R$. Here V, N and R are the atomic volume, Avogadro's number and the gas constant, respectively.

One can immediately see that with an increase in atomic volume during the process of crystallization, the nucleation rate will be reduced. This is possibly what is happening with the $Pd_{40}Ni_{40}P_{20}$ and the $Pd_{30}Ni_{50}P_{20}$ glasses for which Chen et al. [43] report a reduction in density upon crystallization (Figure 5-13).

7.3 Chemical Bonding:

We have investigated the possibility that chemically the ternary $Pd_xNi_{(80-x)}P_{20}$ glasses are composed of Pd_3P and Ni_3P – like local environments. We have

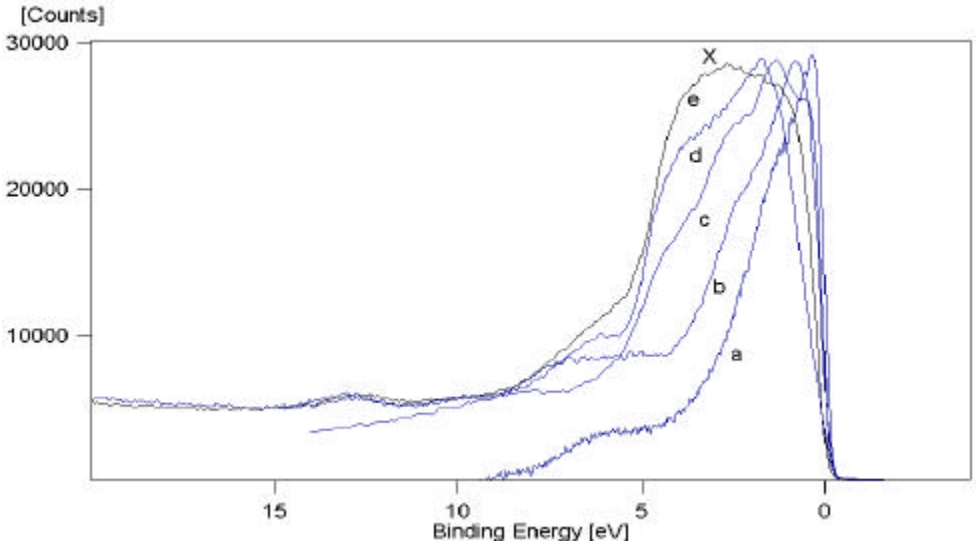

Figure 7-3: The valence band DOS of a) Ni, b)$Ni_{80}P_{20}$ glass, c) Pd, d) Pd_3P crystal, and e) $Pd_{40}N_{40}P_{20}$ glass. The spectra are scladed to match their maximum intensities.

considered the valence band structure of the binary alloys of $Ni_{80}P_{20}$ and Pd_3P as possible components of the valence band structure of $Pd_xNi_{(80-x)}P_{20}$. Fig. 7-3 shows the development of the valence band DOS upon alloying Ni, Pd and P. The overall width of the valence band is greatly increased when Pd is added in $Ni_{80}P_{20}$ (Fig. 7-3b) to make $Pd_{40}Ni_{40}P_{20}$ (Fig. 7-3e).

A similar broadening has been also suggested by theoretical band structure calculations for glassy $Pd_{40}Ni_{40}P_{20}$ in which Pd atoms are substituted for Ni atoms in

the $Ni_{80}P_{20}$ structure [52] (Figure 7-4). In these calculations, the structural origins of these X seem to be a result of new states in Pd.

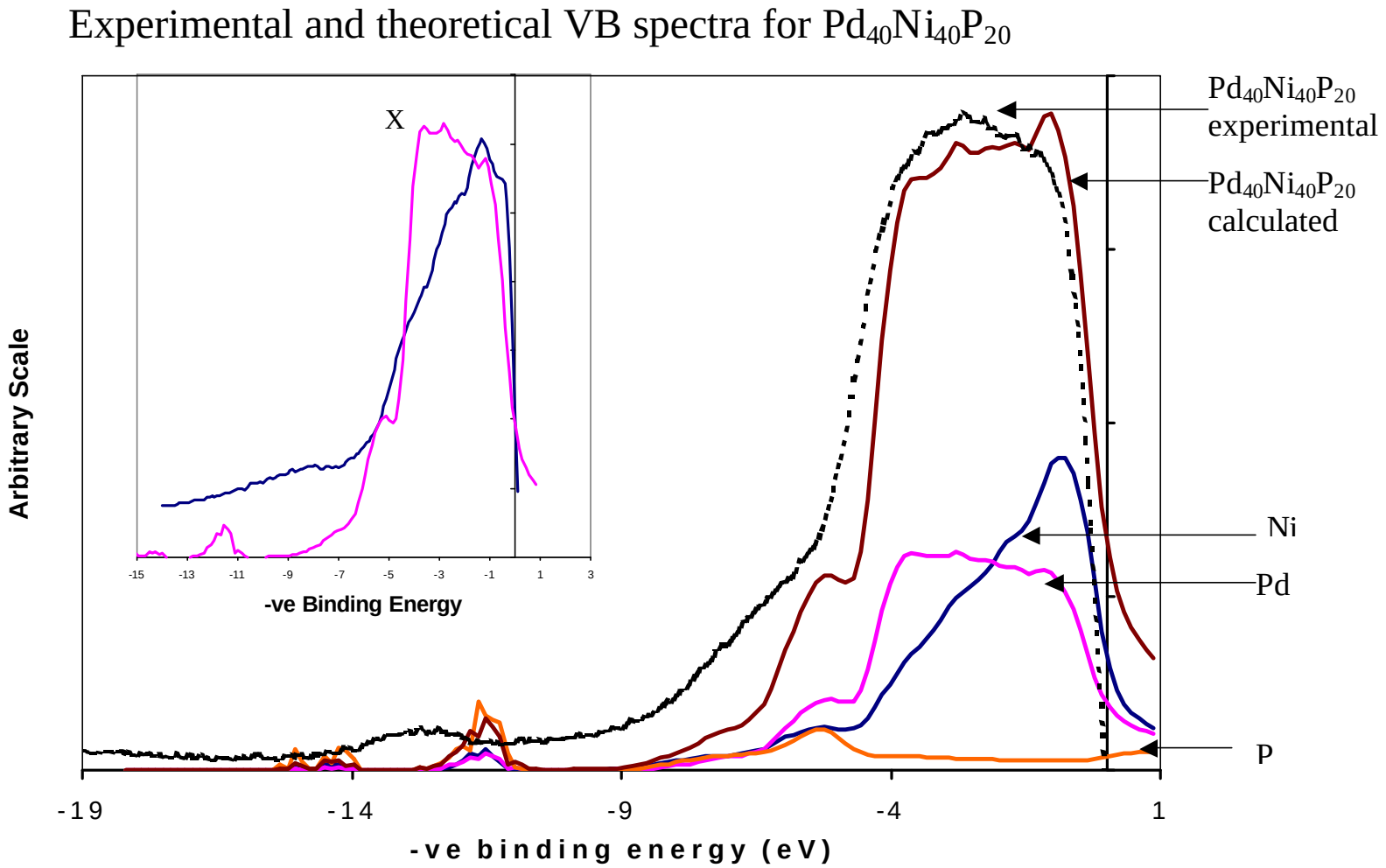

Figure 7-4 : The valence band for the $Pd_{40}Ni_{40}P_{20}$ glass calculated using the $Ni_{80}P_{20}$ starting structure in a locally self-consistent multiple scattering (LSMS) scheme[52]. The inset shows the Pd local DOS (LDOS) in this alloy . Clearly the result of alloying is a broadening of the d-band of Pd and that the state marked X originate from Pd.

Looking back at Figure 7-3, insofar as the breadth of the band is concerned, the valence band of Pd_3P is closer than that of $Ni_{80}P_{20}$ to the valence band of the ternary glass. More interestingly, note that compositionally weighted linear combinations of the binary DOS can not simulate the DOS of the ternary glass $Pd_{40}Ni_{40}P_{20}$ in the region marked X (~ 3.5 - 4.5 eV). This extra valence band structure is a unique feature of these BMGs.

It has been observed by Miller *et al.* [53] by atom probe field ion microscopy that $Pd_{40}Ni_{40}P_{20}$ glass decomposes into three distinguishable phases upon crystallization, viz., $Pd_{28}Ni_{48}P_{24}$, $Pd_{69}Ni_9P_{22}$ and an fcc phase of $Pd_{45}Ni_{40}P_{15}$. The implication of these results is that the crystalline $(Pd,Ni)_{80}P_{20}$ is not simply a solid solution of Ni_3P and Pd_3P- like phases, but that some stable crystal structures exist at the intermediate compositions. The question, therefore, remains as to how closely the ternary glasses in this system follow the atomic and crystalline structure of the crystals, and how this affects the glass-stability of the intermediate compositions.

As we know, $Pd_{30}Ni_{50}P_{20}$ and $Pd_{60}Ni_{20}P_{20}$ mark the limits of BMG formation. The former is close compositionally to the first crystalline phase identified by Miller *et al.* to exist in crystallized $Pd_{40}Ni_{40}P_{20}$. The latter approaches the composition of the second phase. If we expect that the structure of $Pd_{40}Ni_{40}P_{20}$ glass follows that of its crystalline counterpart, then its structure should be an average of those glasses with $Pd_{30}Ni_{50}P_{20}$ and $Pd_{70}Ni_{10}P_{20}$ nominal composition. For the same reason, we should be able to construct the valence band of glassy $Pd_{40}Ni_{40}P_{20}$ from a linear combination of

the DOS of glassy $Pd_{30}Ni_{50}P_{20}$ and $Pd_{70}Ni_{10}P_{20}$. Since $Pd_{70}Ni_{10}P_{20}$ is outside the glass forming range, for our simulation we used $Pd_{60}Ni_{20}P_{20}$ as the closest glass. Indeed we find ($2/3 \bullet DOS_{Pd30Ni50P20} + 1/3 \bullet DOS_{Pd60Ni20P20}$) simulates the experimental

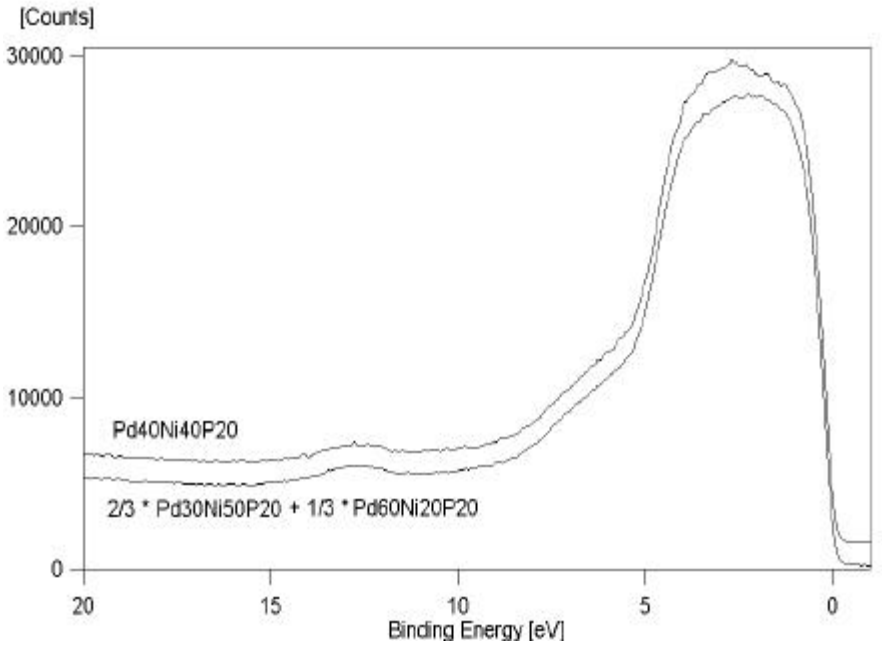

Figure 7-5: A comparison of the valence band of $Pd_{40}Ni_{40}P_{20}$ and that of a simulated spectrum using a weighted average of $Pd_{60}Ni_{20}P_{20}$ and of $Pd_{30}Ni_{50}P_{20}$

$DOS_{Pd40Ni40P20}$ quite accurately (Figure 7-5). Thus, the electronic structure of the most stable glass in the $Pd_xNi_{(80-x)}P_{20}$ system, $Pd_{40}Ni_{40}P_{20}$, is in fact an average of the electronic structure of $Pd_{60}Ni_{20}P_{20}$ and $Pd_{30}Ni_{50}P_{20}$ glasses.

Similar attempts fail to simulate the valence band DOS of $Pd_{60}Ni_{20}P_{20}$ and $Pd_{30}Ni_{50}P_{20}$ using any one of the binary alloy DOS ($Ni_{80}P_{20}$ or Pd_3P) along with that of $Pd_{40}Ni_{40}P_{20}$ [54, 55]. This confirms that chemical bonding in bulk glass formation range of the $Pd_xNi_{(80-x)}P_{20}$ system, $30 \leq x \leq 60$, is qualitatively different from those of the binary alloys.

Let us look back at the core-level binding energies for Ni, Pd and P as a function of composition of glasses and crystals in the $Pd_xNi_{(80-x)}P_{20}$ system (Table 6-1). We can examine which glass in the series has the closest chemical bonding with respect to its of the corresponding crystal. Fig. 7-6 shows this characteristically for core level binding energies. The relative errors estimated for the XPS setup used was > 0.03 eV [56]. Here, 0.02 eV error is used to display the band of possible core-level shifts for both the glassy and crystalline cases. We can, therefore, encompass a large range of possible points of intersection between the trend-lines for the glasses and the crystals from ~ 36.5 % to about 68.9 % Pd. The closest electronic structure between a glass and its corresponding crystal in $Pd_xNi_{(80-x)}P_{20}$ system is occurs at ~ $Pd_{53}Ni_{27}P_{20}$ composition, which, is close to the Pd rich end of BMG formation. That is, from an electronic structure point of view, the $Pd_{60}Ni_{40}P_{20}$ glass is closer to its crystalline counterpart than are $Pd_{40}Ni_{40}P_{20}$ and $Pd_{30}Ni_{50}P_{20}$ glasses. This substantiates what we have already observed through EXAFS from the changes in the local environment around the transition metals upon crystallization.

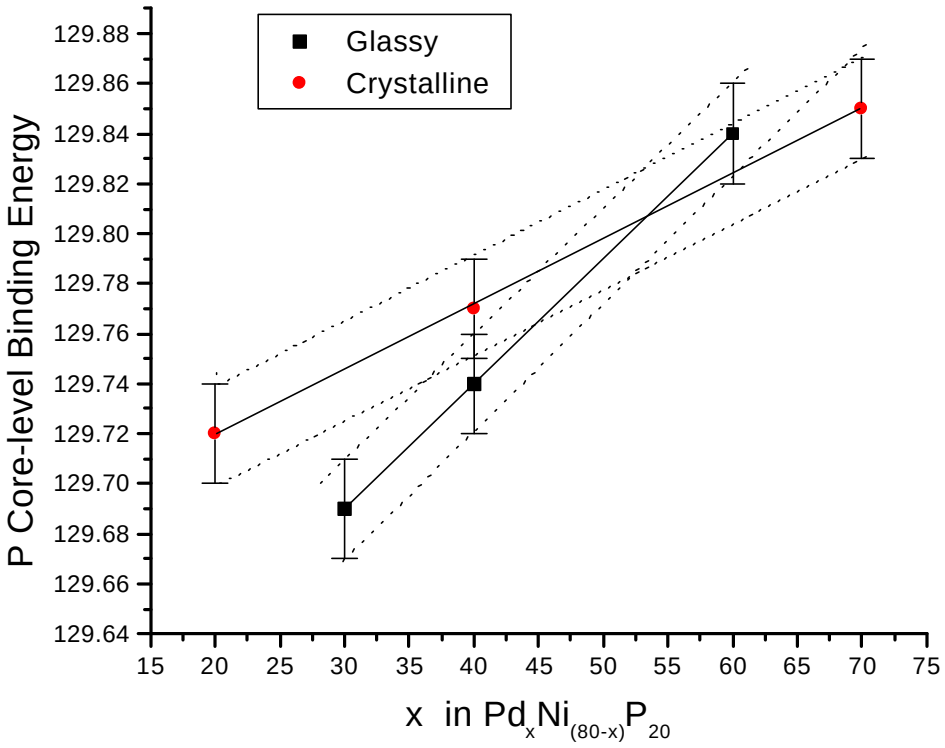

Figure 7-6: The P $2p_{3/2}$ core level positions of the glasses and crystals in the $Pd_xNi_{(80-x)}P_{20}$ glass.

7.4 Nagel and Tauc Criterion

A quasicrystalline phase, characterized by a five-fold rotational symmetry but no long-range order, is known to be stabilized by conduction electrons. A dip-like anomaly was reported in the DOS at E_F [57] which has been claimed to stabilize to the quasicrystalline phase.

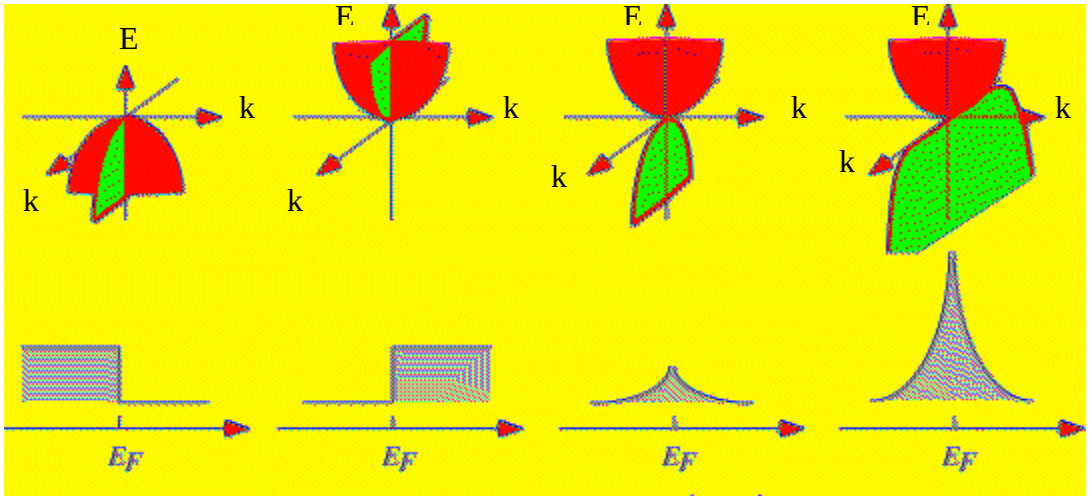

Figure 7-7: Schematic showing the how creation of saddle points in the E-k dispersion can cause singularities in the DOS driving it away from the Fermi-Dirac ideal.

To gain an understanding of the reasons why a dip, or a pseudo-gap in the Fermi level can give rise to electronic stability we have to first ask how such singularities originate. Van Hove [58] had shown that in a two-dimensional system a saddle point in the momentum dispersion can cause logarithmic divergences in the DOS (Figure 7-7). If all the states up to infinite energy would be occupied, then these pseudo-gaps would have no effect on the total energy, since a dip in the DOS (away

from, let us say, a free electron ideal) would be counterbalanced by a peak elsewhere (Figure 7-8). However, if there is a dip in the DOS at E_F, $D(E_F)$, corresponding peaks must lie above E_F and are not accessed by the ground state electrons and results in an

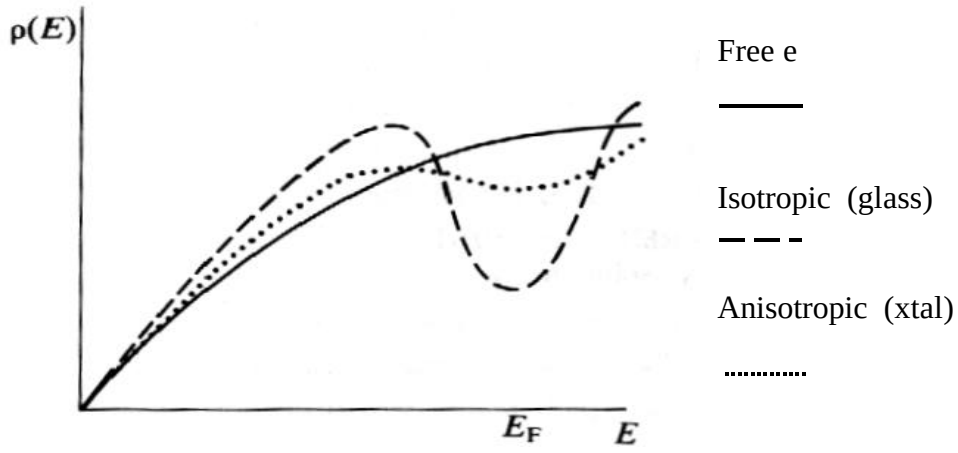

Figure 7-8: A schematic of the DOS of free electrons in a metal, and those in metallic glass and its corresponding crystal.

overall stabilization of the system. Electronic states get raised or depressed at zone boundaries creating anomalies in the DOS similar to Van Hove singularities, and so, when Brillouin zone boundaries and the Fermi sphere overlap, this electronic stabilization is expected to be the greatest.

Various ideas have been proposed for increased stability of the overall alloy, or specifically the glassy alloy with respect to that of the crystal. Most of these involve some form of a constructive interference between the peak in the structure factor, $S(q)$, as obtained from a diffraction experiment, with the surface of the Fermi sphere. That is, $S_p(q)$, the peak positions in the structure factor is twice the Fermi wave vector; $S_p(q) = 2k_F$.

In the free electron approximation it can easily be derived that we know that:

$$k_F = \left(3\pi^2 \frac{\dot{Z} N}{V} \right)^{\frac{1}{3}} \qquad [7.4]$$

where N is Avogadro's number and V is the molar volume, and $\bar{}$ is the average valence electron concentration, or the nominal number of electrons per atom in the valence band calculated simply as $\bar{} = (pe_c + qe_a)/(p+q)$, where p and q are the concentrations of cations and anions and e_c and e_a are the numbers of valence electrons of the cations and anions, respectively.

The relevance of the super-positioning of k_F with peaks in the structure factor to the stability of metallic glass was explored by Nagel and Tauc [59]. They extended concepts of Ziman's theory of liquid metals to the case of metallic glass. Nagel and Tauc argue that a metallic glass where the Fermi sphere touches the pseudo-Brillouin zone should be more stable against crystallization than a glass where this does not happen. This is because the deep minimum in $D(E_F)$ requires the first pseudo-Brillouin zone to be as spherically symmetric as possible, so that its overlap with the Fermi sphere, and this isotropy is destroyed by the process of crystallization.

We have examined the relationship between the $D(E_F)$ and the known stabilities of the $Pd_xNi_{(80-x)}P_{20}$ glasses. Over the composition range, $D(E_F)$ is difficult to compare partly because the Fermi levels themselves are shifting, and partly because of the different photoionization cross-sections for the valence electrons of the different constituent elements. There is an indirect method for comparing the electron

occupancy at the Fermi level (Briggs and Seah 1983)[60]. When an electron is ejected from a core level, it can perturb the valence-band, which is manifested in the excitation of electrons to the conduction band. The probability for the occurrence of this event is determined by the level of occupancy of electrons at the Fermi level. These excitations reduce the kinetic energy of the ejected core electrons and leave a tailing effect on the high binding energy side of the core level peak. The larger the resulting asymmetry of a core-level peak, the greater is the occupancy at the Fermi level. Based on this understanding the degree of asymmetry was determined in the Ni $2p_{3/2}$ core-level peaks. A Voigt function, which is a linear mix of a symmetric

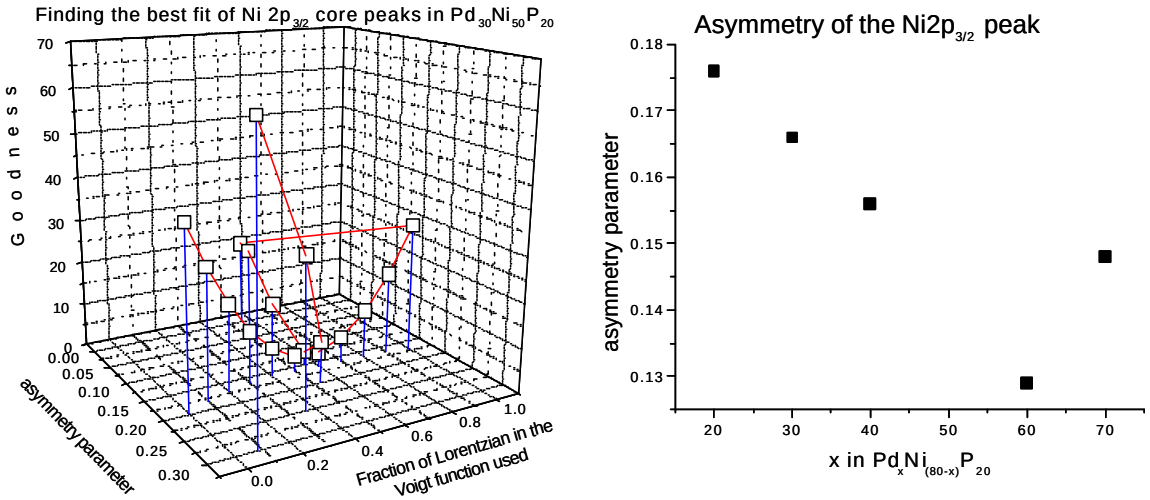

Figure 7-9: a) an example of the multiple fits carried out in order to avoid correlations, and b) the asymmetry parameter for the different alloy compositions.

Gaussian and a Lorentzian with variable asymmetry, was used. Curve fitting required that highly correlated parameters, in this case, the mixing coefficient and the

asymmetry parameter, were not allowed to run free simultaneously (Figure 7-9a). It was found by curve fitting that indeed the asymmetry for the g-$Pd_{30}Ni_{50}P_{20}$ alloy was higher than that for the g-$Pd_{40}Ni_{40}P_{20}$ one, which is consistent with the Nagel and Tauc criterion (Figure 7-9b). However, the minimum asymmetry does *not* occur at the g-$Pd_{40}Ni_{40}P_{20}$ composition but rather at g-$Pd_{60}Ni_{20}P_{20}$. The asymmetry increased once again, beyond the bulk glass formation range of composition, for the $Pd_{70}Ni_{10}P_{20}$ alloy. The highest glass stability of the g-$Pd_{40}Ni_{40}P_{20}$ alloy in the composition range is not reflected in a minimum in $D(E_F)$ for this alloy. So, a minimum in $D(E_F)$ has been found for the $Pd_{60}Ni_{20}P_{20}$ glass, but this still indicates an alloy stability and not necessarily a glass stability. Unfortunately, the $D(E_F)$ for a recrystallized $Pd_{60}Ni_{20}P_{20}$ is not available.

7.5 Valence Electron Concentration (VEC) Effect

The peak in the structure factor, on the other hand depends on the average valence electron concentration (VEC), $\bar{}$. In fact, Nagel and Tauc showed that this peak position scales with $\bar{}$. It has been suggested by Haüssler [61] that a $\bar{}$ of 1.8 e/a ensures an optimal positioning of the peak in the structure factor with respect to the surface of the Fermi sphere. Putting in $\bar{}_{alloy}$=1.8 we can calculate the optimal alloy composition for this stability. For this simple calculation, however, one must assume

a VEC for all the elements in the system. If we use the nominal, ground state $^{-}$ for the elements, i.e., $^{-}_{Pd}$=0, $^{-}_{Ni}$=2 and $^{-}_{P}$=5, thenfor the $Pd_xNi_{(80-x)}P_{20}$ we can solve for x:

$$\{x(0) + (80-x)(2) + (20)(5)\}/100 = 1.8 \qquad [7.4]$$

which gives us the solution of x=0.4, giving us the $Pd_{40}Ni_{40}P_{20}$ alloy. It is not likely that $^{-}_{Pd}$ = 0, and that $^{-}_{Ni}$ = 2. We have observed that the entire valence bands of TM-P alloys are shifted with respect to elemental TM ones, indicating that a charge transfer is taking place between P and the TMs. Further, since we observe some states in the valence band of only the ternary alloys, we should assume that, with the mixing of Pd and Ni to produce the ternary glass, some charge transfer takes place between Pd and Ni atoms. This would shift the VEC of Ni and Pd away from their nominal values.

We can attempt to back-calculate the VEC, assuming that the total VEC of Pd+Ni remains 2 and that the VEC of P is 5, and further assuming that the VEC is the same for the two compositions at the end of BMG formation. The first assumption tells us that we are only allowing for a charge transfer between Pd and Ni atoms. The second assumption, that the two end compositions of BMG formation $Pd_{30}Ni_{50}P_{20}$ and the $Pd_{60}Ni_{20}P_{20}$ have the same VEC, implies that VEC is forced to stay constant throughout the BMG formation range, allowing a proper matching of k_F with the first peak in the structure factor. This is not unreasonable since we observed in both the Pd and Ni the near-edge structure no shift in the band, and the oscillations remained in phase throughout the composition (Figures 5-2,7).

We can then construct the following equalities:

$0.6x + 0.2\,(2-x) + 0.2\,(5) = \bar{}$ [7.5]

and

$0.3x + 0.5\,(2-x) + 0.2\,(5) = \bar{}$ [7.6]

Solving equations 7.5 and 7.6 for $\bar{}$ gives us $\bar{}$ = 1.8. Thus, our assumptions are validated.

Looking at equation 7.4, it seems that a change in $\bar{}$ should not affect the position of k_F very sharply since k_F increases only as the cube root of $\bar{}$. However, we are describing a system which is already very close to its thermodynamic equilibrium, and so even small changes in $\bar{}$ could effectively push the system away from its glass formation region.

Unfortunately, in order to match the peak positions of our k-space information with calculated k_F values, we need an accurate determination of E_F on the EXAFS edge, and we do not know that absolutely. Also, even though $\div(k)$ is related to $S_p(q)$ [62] the comparison fails in the region of k< ~ 2.5 $Å^{-1}$, because the final-state electrons at these low energies have long mean free paths, leading to multiple-atom scattering. It is therefore not useful to speak of peaks in valleys in the $\div(k)$ in this region, in the same manner as one would for $S_p(q)$. We can, however, calculate, using k_F, the position of the minima in the pair potential function, and compare these minima to the peak positions in real-space.

7.6 Size effect

Hafner [63] proposed a theory whereby the phase, whether glassy or crystalline will be stabilized when the peaks in pair distribution functions coincide with the minima in the inter-atomic pair potential function. The pair potential he uses has the form

$$V(r) = A\{\sin(2k_F * R)/R^3\} \qquad [7.7]$$

Using k_F calculated by equation 7.4, where the molar volumes of the $Pd_{60}Ni_{20}P_{20}$ and the $Pd_{30}Ni_{50}P_{20}$ glasses are used, we can calculate the V(r) function

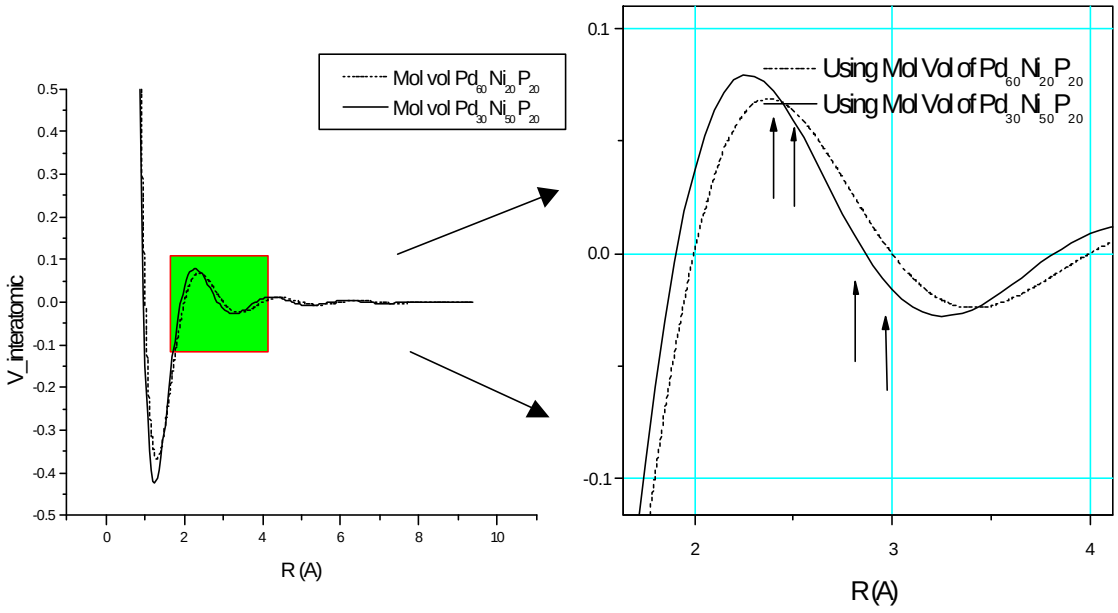

Figure 7-10: V(r) for the molar volumes of $Pd_{60}Ni_{20}P_{20}$ and $Pd_{30}Ni_{50}P_{20}$ and $\bar{}$=1.8. The arrows mark the range of TM-P and TM-TM distances, Ni-P, Pd-P, Ni-Ni and Pd-Pd, respectively, for the Pd_3P and the Ni_3P alloys. The values are ~2.35 Å, 2.48 Å, 2.77 Å and 2.93 Å, respectively.

using equation 7.7, for these two glasses, respectively. In Figure 7-10 we observe the effect of $^{-}$ and the molar volume, on the minimum in V(r).

It is clear that the decrease in molar volume as Ni concentration increases, is pushed to a lower distance. The molar volume of $Pd_{30}Ni_{50}P_{20}$ places a deeper potential at all the nearest neighbor distances, and so is a more stable structure based on the size effects only. On the other hand, Pd-P neighbors are at a lower potential than the Ni-P ones for either molar volumes, and the same is true for the Pd-Pd neighbors, versus the Ni-Ni ones. This is consistent with what we observe upon crystallization where the Ni-Ni nearest neighbors are seen to undergo a more dramatic change than Pd-Pd ones.

8 Conclusions

We have shown that the stability of the Pd-Ni-P bulk metallic glasses depend on the interaction of both the atomic and electronic effects on the structure. The $Pd_xNi_{(80-x)}P_{20}$ system was selected because it is the starting composition for the best known bulk metallic glass former and because it is representative of a whole class of BMGs. At the same time with only three elements, a study of the structural response to composition change and the interpretations of these changes from the point of view of glass-stability, remains tractable in the $Pd_xNi_{(80-x)}P_{20}$ system.

In the composition range of the $Pd_xNi_{(80-x)}P_{20}$ system, the ends of bulk glass formability are marked by $Pd_{30}Ni_{50}P_{20}$ and $Pd_{60}Ni_{20}P_{20}$ glasses. These two ternary glasses have been shown to be isostructural to Ni_3P and Pd_3P binary crystalline alloys, respectively. The atomic and electronic structure of $Pd_{40}Ni_{20}P_{20}$ composition, which is the best glass former in this composition range, is a simple weighed sum of those of $Pd_{60}Ni_{20}P_{20}$ and $Pd_{30}Ni_{50}P_{20}$ glasses.

The trigonal prism structure, which is one of the larger holes predicted by Bernal in his analysis of a dense, random packing of hard spheres, occurs naturally in both the Pd_3P and Ni_3P structures and, by extension, in the Pd-Ni-P glasses. The densely packed structure of the glass is stabilized by the fact that alternative crystalline phases are themselves not very stable due to frustration of three-dimensional space.

Nagel and Tauc had proposed that a valence electron concentration of 1.8 e/a ensures the super-positioning of the first peak in the structure factor with twice the Fermi vector and stabilizing a metallic glass system through a lowering of the DOS at the Fermi level. From XPS, we have demonstrated that the DOS at the Fermi level in the ternary $Pd_xNi_{(80-x)}P_{20}$ glasses are lower than those of the binary alloys near the composition end, consistent with the Nagel and Tauc criterion. However, the minimum in the DOS is not found to occur at $Pd_{40}Ni_{40}P_{20}$, the composition best suited for glass formation, but rather at $Pd_{60}Ni_{20}P_{20}$.

Using the valence electron concentration of 1.8 e/a, the interatomic potential of the alloys were calculated. We found from EXAFS that the Pd nearest neighbors are placed at more attractive positions in the interatomic potential than are Ni ones. However, the molar volume of $Pd_{30}Ni_{50}P_{20}$ places all the nearest neighbor distances nearer to a minimum in the interatomic potential. Chemical bonding, as revealed by new states in the valence band (from XPS) that are present only in the ternary alloys, points to a further stabilization of the system through a negative heat of mixing between Pd and Ni atoms.

Next, the stability of $Pd_xNi_{(80-x)}P_{20}$ glasses was investigated from the point of view of their resistance to crystallization. It is proposed that the $Pd_{60}Ni_{20}P_{20}$ glass is stabilized against crystallization through a low enthalpy component to the Gibbs free energy. We conclude this based on our observation that the crystallization of this glass requires a minimum amount of rearrangement in the metal environment. The $Pd_{30}Ni_{50}P_{20}$ and $Pd_{40}Ni_{40}P_{20}$ glasses are stabilized against crystallization, we propose,

through a large entropy change upon crystallization because the crystallization of these alloy involves a large ordering of the local atomic structure. The $Pd_{40}Ni_{40}P_{20}$ glass receives additional stability against crystallization due to the kinetic hindrances imposed by having to create both a Ni rich as well as a Pd rich phase close to the compositions of Ni_3P and Pd_3P.

The stability of Pd-Ni-P bulk metallic glasses originates from cumulative and interrelated effects, both atomic (packing efficiency, low symmetry) as well as electronic (pseudo-gap near the Fermi level, chemical bonding and valence electron concentration).

9 Appendix A

The parameters for the various coordination shells of the Pd_3P structure used in the fit are given below. At the bottom is located a part of the correlation matrix showing a high correlation between parameters 1 and 4. These are the S_0^2 and the $sigma^2$ parameters, which we know are correlated. During the fit, these two parameters were not allowed to vary simultaneously. If they were allowed to vary simultaneously, then at least one of the parameters was made to vary within a narrow range. As we see, in these last 50 iterations, the S_0^2 parameter was allowed to vary only between 0.8 and 1. A fit was deemed acceptable if the reduced chi-squared value was < 100.

```
Iterations:    50
(CHI)'2:       26552.307
Residual:      15.013313
Exp.Error:     1.172E-005
chi2 w/o err:  2.7360759E-006
reduced chi2:  84.026288
data points:   321
Lambda:        0.01
termination:   1E-005
Delta(part.):  1E-005

Fit carried out in R space.
   Bottom border: 0
   Top border:    3.10375
   k range from   1.8699  to  15.986
Number of independent parameters   :  28.8
Number of free running parameters  :  6

Number of single scattering paths  :  20
Number of multiple scattering paths:  0

  Weight for FEFF file No. 1 :  0.16667
  Weight for FEFF file No. 2 :  0.16667
  Weight for FEFF file No. 3 :  0.33333
```

```
  Weight for FEFF file No. 4 :  0.33333

----------------------------

 feff cluster fit:
  xyz-Coeff. #1: -0.015052391
  xyz-Coeff. #2: -0.014285256
  xyz-Coeff. #3: -0.042121761
.............................

   Einstein Temperature:   350.71066 K

  FT Mag + Imag. saved as 4-col ascii file:
   'XAFS_FT_i_mag.dat'

.............................                   initial parameter
 feff-S0
.............................
#1  S0^2:         0.8259871     +- 0.00161976          0.82304
CONSTRAIN from : 0.8 to : 1
-----------------------------
 feff-Fit  - feff0001.dat, Pd - P
.............................
#2  Coord.No.:    2             +- 0                   2         FIXED
#3  distance R:   2.273203      +- 0                   2.3079    FIXED
xyz lattice correlated
#4  sigma^2:      0.005481019   +- 1.75047             351.080
#5  E0 shift:    -2.589896      +- 0.0139738           -2.5390
-----------------------------
 feff-Fit  - feff0002.dat, Pd - P
.............................
#6  Coord.No.:    1             +- 0                   1         FIXED
#7  distance R:   3.094446      +- 0                   3.1417    FIXED
xyz lattice correlated
#8  sigma^2:      0.005481019   +- 0                   0.00547
FIXED
#9  E0 shift:    -2.589896      +- 0                   -2.5390
CORRELATED to #5 * 1
-----------------------------
 feff-Fit  - feff0001.dat, Pd - Pd
.............................
#10 Coord.No.:    2             +- 0                   2         FIXED
#11 distance R:   2.803732      +- 0                   2.8444    FIXED
xyz lattice correlated
#12 sigma^2:      0.002471695   +- 0                   0.00246
FIXED
#13 E0 shift:    -2.589896      +- 0                   -2.5390
CORRELATED to #5 * 1
-----------------------------
 feff-Fit  - feff0002.dat, Pd - Pd
.............................
#14 Coord.No.:    2             +- 0                   2         FIXED
```

```
#15 distance R:   2.874578      +- 0                    2.9162   FIXED
xyz lattice correlated
#16 sigma^2:      0.002471695   +- 0                    0.00246
FIXED
#17 E0 shift:    -2.589896      +- 0                    -2.5390
CORRELATED to #5 * 1
-----------------------------
 feff-Fit  - feff0003.dat, Pd - Pd
.............................
#18 Coord.No.:    2             +- 0                    2        FIXED
#19 distance R:   2.886055      +- 0                    2.9279   FIXED
xyz lattice correlated
#20 sigma^2:      0.002471695   +- 0                    0.00246
FIXED
#21 E0 shift:    -2.589896      +- 0                    -2.5390
CORRELATED to #5 * 1
-----------------------------
 feff-Fit  - feff0004.dat, Pd - Pd
.............................
#22 Coord.No.:    2             +- 0                    2        FIXED
#23 distance R:   2.887617      +- 0                    2.9295   FIXED
xyz lattice correlated
#24 sigma^2:      0.002471695   +- 0                    0.00246
FIXED
#25 E0 shift:    -2.589896      +- 0                    -2.5390
CORRELATED to #5 * 1
-----------------------------
 feff-Fit  - feff0005.dat, Pd - Pd
.............................
#26 Coord.No.:    2             +- 0                    2        FIXED
#27 distance R:   3.168095      +- 0                    3.214    FIXED
xyz lattice correlated
#28 sigma^2:      0.002471695   +- 0                    0.00246
FIXED
#29 E0 shift:    -2.589896      +- 0                    -2.5390
CORRELATED to #5 * 1
-----------------------------
 feff-Fit  - feff0006.dat, Pd - Pd
.............................
#30 Coord.No.:    2             +- 0                    2        FIXED
#31 distance R:   3.175973      +- 0                    3.222    FIXED
xyz lattice correlated
#32 sigma^2:      0.002471695   +- 0                    0.00246
FIXED
#33 E0 shift:    -2.589896      +- 0                    -2.5390
CORRELATED to #5 * 1
-----------------------------
 feff-Fit  - feff0001.dat, Pd - P
.............................
#34 Coord.No.:    1             +- 0                    1        FIXED
#35 distance R:   2.22074       +- 0                    2.3184   FIXED
xyz lattice correlated
```

```
#36 sigma^2:      0.005481019   +- 0                  0.00547
FIXED
#37 E0 shift:    -2.589896      +- 0                  -2.5390
CORRELATED to #5 * 1
-----------------------------
 feff-Fit  - feff0002.dat, Pd - P
.............................
#38 Coord.No.:    1             +- 0                  1        FIXED
#39 distance R:   2.286982      +- 0                  2.3876   FIXED
xyz lattice correlated
#40 sigma^2:      0.005481019   +- 0                  0.00547
FIXED
#41 E0 shift:    -2.589896      +- 0                  -2.5390
CORRELATED to #5 * 1
-----------------------------
 feff-Fit  - feff0003.dat, Pd - P
.............................
#42 Coord.No.:    1             +- 0                  1        FIXED
#43 distance R:   2.488188      +- 0                  2.5976   FIXED
xyz lattice correlated
#44 sigma^2:      0.005481019   +- 0                  0.00547
FIXED
#45 E0 shift:    -2.589896      +- 0                  -2.5390
CORRELATED to #5 * 1
-----------------------------
 feff-Fit  - feff0001.dat, Pd - Pd
.............................
#46 Coord.No.:    1             +- 0                  1        FIXED
#47 distance R:   2.660727      +- 0                  2.7777   FIXED
xyz lattice correlated
#48 sigma^2:      0.002471695   +- 0                  0.00246
FIXED
#49 E0 shift:    -2.589896      +- 0                  -2.5390
CORRELATED to #5 * 1
-----------------------------
 feff-Fit  - feff0002.dat, Pd - Pd
.............................
#50 Coord.No.:    1             +- 0                  1        FIXED
#51 distance R:   2.724555      +- 0                  2.8444   FIXED
xyz lattice correlated
#52 sigma^2:      0.002471695   +- 0                  0.00246
FIXED
#53 E0 shift:    -2.589896      +- 0                  -2.5390
CORRELATED to #5 * 1
-----------------------------
 feff-Fit  - feff0003.dat, Pd - Pd
.............................
#54 Coord.No.:    1             +- 0                  1        FIXED
#55 distance R:   2.747264      +- 0                  2.8681   FIXED
xyz lattice correlated
#56 sigma^2:      0.002471695   +- 0                  0.00246
FIXED
```

```
#57 E0 shift:    -2.589896      +- 0                    -2.5390
CORRELATED to #5 * 1
----------------------------
 feff-Fit  - feff0004.dat, Pd - Pd
.............................
#58 Coord.No.:    2             +- 0                    2         FIXED
#59 distance R:   2.76091       +- 0                    2.8823    FIXED
xyz lattice correlated
#60 sigma^2:      0.002471695   +- 0                    0.00246
FIXED
#61 E0 shift:    -2.589896      +- 0                    -2.5390
CORRELATED to #5 * 1
----------------------------
 feff-Fit  - feff0005.dat, Pd - Pd
.............................
#62 Coord.No.:    1             +- 0                    1         FIXED
#63 distance R:   2.7934        +- 0                    2.9162    FIXED
xyz lattice correlated
#64 sigma^2:      0.002471695   +- 0                    0.00246
FIXED
#65 E0 shift:    -2.589896      +- 0                    -2.5390
CORRELATED to #5 * 1
----------------------------
 feff-Fit  - feff0006.dat, Pd - Pd
.............................
#66 Coord.No.:    1             +- 0                    1         FIXED
#67 distance R:   2.804553      +- 0                    2.9279    FIXED
xyz lattice correlated
#68 sigma^2:      0.002471695   +- 0                    0.00246
FIXED
#69 E0 shift:    -2.589896      +- 0                    -2.5390
CORRELATED to #5 * 1
----------------------------
 feff-Fit  - feff0007.dat, Pd - Pd
.............................
#70 Coord.No.:    1             +- 0                    1         FIXED
#71 distance R:   2.806071      +- 0.000499779          2.9295  xyz
lattice correlated
#72 sigma^2:      0.002471695   +- 0                    0.00246
FIXED
#73 E0 shift:    -2.589896      +- 0                    -2.5390
CORRELATED to #5 * 1
----------------------------
 feff-Fit  - feff0008.dat, Pd - Pd
.............................
#74 Coord.No.:    2             +- 0                    2         FIXED
#75 distance R:   2.976603      +- 9.2312E-005          3.1075  xyz
lattice correlated
#76 sigma^2:      0.002471695   +- 0                    0.00246
FIXED
#77 E0 shift:    -2.589896      +- 0                    -2.5390
CORRELATED to #5 * 1
```

```
----------------------------
 feff-Fit  - feff0009.dat, Pd - Pd
..........................
#78 Coord.No.:    1            +- 0                  1        FIXED
#79 distance R:   3.078628     +- 5.94874E-005       3.214   xyz
lattice correlated
#80 sigma^2:      0.002471695  +- 0                  0.00246
FIXED
#81 E0 shift:    -2.589896     +- 0                  -2.5390
CORRELATED to #5 * 1
----------------------------
```

Pair	CN	R	sig^2	E0	w(%)
Pd - P	2	2.273	0.00548	-2.59	75.42
Pd - P	1	3.094	0.00548	-2.59	14.62
Pd - Pd	2	2.804	0.00247	-2.59	49.13
Pd - Pd	2	2.875	0.00247	-2.59	45.57
Pd - Pd	2	2.886	0.00247	-2.59	45.27
Pd - Pd	2	2.888	0.00247	-2.59	45.23
Pd - Pd	2	3.168	0.00247	-2.59	34.14
Pd - Pd	2	3.176	0.00247	-2.59	33.94
Pd - P	1	2.221	0.00548	-2.59	82.11
Pd - P	1	2.287	0.00548	-2.59	74.56
Pd - P	1	2.488	0.00548	-2.59	60.56
Pd - Pd	1	2.661	0.00247	-2.59	55.39
Pd - Pd	1	2.725	0.00247	-2.59	52.38
Pd - Pd	1	2.747	0.00247	-2.59	50.65
Pd - Pd	2	2.761	0.00247	-2.59	100
Pd - Pd	1	2.793	0.00247	-2.59	49.08
Pd - Pd	1	2.805	0.00247	-2.59	48.57
Pd - Pd	1	2.806	0.00247	-2.59	48.49
Pd - Pd	2	2.977	0.00247	-2.59	81.44
Pd - Pd	1	3.079	0.00247	-2.59	36.76

- Correlation matrix :

	1	4	71	75	79
1	1	-0.7571	-0.2563	0.03916	0.08948
4	-0.7571	1	0.1879	0.335	0.02383
71	-0.2563	0.1879	1	0.09907	0.003574
75	0.03916	0.335	0.09907	1	0.6196
79	0.08948	0.02383	0.003574	0.6196	1

82 83 84 85

References

1 L.D. Pye, J.G. O'Keefe, and V.D. Frechette, eds., North-Holland, Amsterdam, 1984.

2 W. Klement, Jr., R.H. Willens, P. Duwez, Nature 187, 869 (1960).

3 M.H. Cohen, D. Turnbull, Nature 189, 131 (1961).

4 B.G. Bagley, F.J. DiSalvo, Amorphous Magnetism, A.M. deGraaf, eds., Plenum, New York, 43, 1973.

5 H.S.Chen, Acta Met. 22, 1505, 1974.

6 H.W. Kui, A.L. Greer and D. Turnbull, Appl. Phys. Lett. 45, 615, 1984.

7 R. Willnecker, K. Wittman, and G.P. Gorler, J. Non-Cryst. Sol. 156-158, 450, 1993.

8 A. Inoue, K. Ohtera, K. Kita & T. Masumoto, Jpn. J. Appl. Phys.27, L2248-L2251 (1988).

9 A. Inoue, T. Zhang, W. Zhang, A. Takeuchi, Mater. Trans. JIM 37, 181 (1996).

10 A. Inoue, T. Zhang, Mater. Trans. JIM 36, 1184 (1995).

11 W. L. Johnson, Mater. Sci. Forum 225-227, 35 (1996).

12 A. Inoue, N. Nishiyama and H.M. Kimura, Mater. Trans. JIM 38, 179 (1997).

13 T.D. Shen, Y. He, R.B. Schwarz, J. Mater. Res. 14, 5, 2107 (1999).

14 A Inoue, Bulk Amorphous Alloys: Practical Characteristics and Applications, Materials Science Foundation 6, Trans. Tech. Publications Ltd., Switzerland, 3 (1999).

15 A. Inoue, T. Nakamura, T. Sugita, T. Zhang, & T. Masumoto, Mater. Trans. JIM 34, 351(1993).

16 Greer, A. L., Nature 366, 303 (1993).

17 A Inoue, Bulk Amorphous Alloys: Preparation and Fundamental Characteristics, Materials Science Foundation 4, Trans. Tech. Publications Ltd., Switzerland, 3 (1998).

18 W.L. Johnson, Mater. Sci. Forum 225-227, 35 (1996).

19 R.B. Schwarz and Y. He, Proc. Int Symp Metastable, Mechanically Alloyed and Nanocrystalline Materials, LANL Publication No.LA-UR-96-1703, Los Alamos National Laboratory, Los Alamos, MN, 1996.

20 He, Y., Schwarz, R. B., Archuleta, J. I., Appl. Phys. Lett. 69, 1861 (1996).

21 Y. He, T. Shen, R.B. Schwarz, Metall Trans. (1998) in press.

22 T.D. Shen, R.B. Schwarz and J.D. Thompson, submitted to J. Appl. Phys.

23 Y. He, R. B. Schwarz, J. I. Archuleta, Appl. Phys. Lett. 69, 1861 (1996).

24 S. Rundqvist, Arkiv Kemi 20, 98 (1963).

25 B. Aronsson, S. Rundqvist, Acta Crys. 15, 985 (1962).

26 J.D. Bernal, Nature 185, 68 (1960).

27 G.S. Cargill, J. Appl. Phys. 41, 12 (1970).

28 P.L. Maitrepierre, J. Appl. Phys. 40, 4826 (1969).

29 Otomo, T., Arai, M., Shibata, K., Suzuki, K., Physica B 213-214, 529-531 (1995).

30 Eisenberger, P., and Kincaid, B.M., 1978, *Science*, **200**, 1441.

31 Stern, E.A., 1978, *Contemporary Phys.*, **19**, 289.

32 Teo, B.K., and Joy, D.C., eds., "EXAFS Spectroscopy: Techniques and Applications", 1981, (New York: Plenum Press).

33 Egerton, R.F. 1996, *Electron Energy-Loss Spectroscopy in the Electron Microscope*, 2nd edn. (New York: Plenum Press), p.247.

34 T.M. Hayes, P.N. Sen, and S.H. Hunter, J. Phys. C 9, 4357 (1976).

35 He, Y., Schwarz, R. B., Archuleta, J. I., Appl. Phys. Lett. 69, 1861 (1996).

36 Personal communication with S. Mehta of OMG Fidelity, Newark, NJ.

37 D. B. Williams, and C. B. Carter, *Transmission Electron Microscopy*, (New York: Plenum Press, 1996) pp. 23.

38 D.A. Shirley, Phys. Rev., B5, 4709 (1972).

39 T. Ressler, J. Phys. IV **7**, 269 (1997).

40 D.E. Sayers and B.A. Bunker, X-ray Absorption, D.C.Koningsberger and R. Prins, eds; Wiley, 1988.

41 T.M. Hayes, J.B Boyce, EXAFS Spectroscopy, Solid State Physics Advances in Research and Applications, H. Ehrenreich, F. Seitz, and D. Turnbull editors, Academic Press, New York, NY, 281 (1982).

42 S. I. Zabinsky, J. J. Rehr, A. Ankudinov, R.C. Albers, and M. J. Eller, Phys. Rev. B 52, 2995 (1995).

43 H.S. Chen, J.T. Krause, E.A. Sigety, J. Non-Cryst. Sol. 13, 321 (1973).

44 U. Harms and R.B. Schwarz, Los Alamos National Laboratory, personal communication.

45 Handbook of X-ray Photoelectron Spectroscopy, Perkin-Elmer Corporation (Physical Electronics Division), 1992.

46 J. L. Finney and J. Wallace, J. Non-Cryst. Sol. 43, 165 (1981).

47 P. H. Gaskell, Glassy Metals II, Topics in Applied Physics 53, 5 (1983).

48 J.L. Finney, Proceedings of the Royal Society A319, 479 (1970).

49 G.S. Cargill III, J. Appl. Phys. 41, 2248 (1970).

50 D.E. Polk, Acta Metall. 20, 485 (1972).

51 D.R. Uhlman, J. Non-Cryst. Sol. **7**, 337 (1972).

52 D.M.C. Nicholson, G.M. Stocks, W.A. Shelton, Y. Wang, J.C. Swihart, Met. And Mat. Trans. 29A, 1845 (1998).

53 M.K. Miller, D.J. Larson, R.B. Schwarz, Y. He, Mat. Sci. Engr. A250, 141 (1998).

54 F.M. Alamgir, H. Jain, A. C.Miller , D. B.Williams, R.B. Schwarz, Phil. Mag. B 79, no. 2, 239 (1999).

55 F. M. Alamgir, H. Jain, R. B. Schwarz, O. Jin and D. B. Williams, J. Non-Cryst. Sol. 274, 1-3, 289 (2000).

56 A.C. Miller, G.W. Simmons, Surface Science Spectra 2, no.1, 55-60 (1993).

57 J.L. Wagner, K.M. Wong and S.J. Poon, Phys. Rev. B 39, 8091 (1989).

58 L. Van Hove, Phys Rev. 89, 1189 (1953).

59 Nagel, S. R. and Tauc, Phys. Rev. Lett., 35, no. 6, 380 (1975).

60 Briggs, D., Seah, M. P., Practical Surface Analysis, John Wiley & Sons Ltd., 1983.

61 P. Haüssler, Interrelation Between Electronic and Ionic Structure in Metallic Glasses, Glassy Metals III, Topics in Applied Physics 72, H. Beck and H.J. Güntherodt eds., Springer-Verlag, Berlin Heidelberg, 163 (1994).

62 P. Eisenberger and G.S. Brown, Sol. State Comm. 29, 481 (1979).

63 J. Hafner, Glassy Metals I, Topics in Applied Physics **46**, H. Beck and H.J. Güntherodt eds., Springer-Verlag, Berlin Heidelberg, 121 (1981).